frontiers | Frontiers in Nanotechnology

TYPE Original Research
PUBLISHED 12 April 2024
DOI 10.3389/fnano.2024.1384605

OPEN ACCESS

EDITED BY
Sarmistha Saha,
GLA University, India

REVIEWED BY
Pradeep Kumar,
University of the Witwatersrand, South Africa
Van-An Duong,
University of Texas Health Science Center at Houston, United States

*CORRESPONDENCE
Mónica C. García,
mgarcia@unc.edu.ar
Paula M. Uberman,
paula.uberman@unc.edu.ar

†These authors have contributed equally to this work and share first authorship

‡These authors have contributed equally to this work and share senior authorship

§These authors have contributed equally to this work and share last authorship

RECEIVED 09 February 2024
ACCEPTED 13 March 2024
PUBLISHED 12 April 2024

CITATION
Torres J, Cadena Castro D, Ancarani R, Bruvera I, Mendoza Zélis P, Martín SE, García MC and Uberman PM (2024), Magnetic hybrid nanomaterial based on a natural polymer and an amino acid as pH/temperature dual-responsive nanoplatform for the delivery of tamoxifen. *Front. Nanotechnol.* 6:1384605. doi: 10.3389/fnano.2024.1384605

Magnetic hybrid nanomaterial based on a natural polymer and an amino acid as pH/temperature dual-responsive nanoplatform for the delivery of tamoxifen

Jazmín Torres[1,2†], Diego Cadena Castro[3,4†], Rosario Ancarani[1], Ignacio Bruvera[5], Pedro Mendoza Zélis[5], Sandra E. Martín[3,4], Mónica C. García[1,2*‡§] and Paula M. Uberman[3,4*‡§]

[1]Universidad Nacional de Córdoba, Facultad de Ciencias Químicas, Departamento de Ciencias Farmacéuticas, Córdoba, Argentina, [2]Consejo Nacional de Investigaciones Científicas y Técnicas, CONICET, Unidad de Investigación y Desarrollo en Tecnología Farmacéutica, UNITEFA, Córdoba, Argentina, [3]Universidad Nacional de Córdoba, Facultad de Ciencias Químicas, Departamento de Química Orgánica, Córdoba, Argentina, [4]Consejo Nacional de Investigaciones Científicas y Técnicas, CONICET, Instituto de Investigaciones en Fisicoquímica de Córdoba, INFIQC, Córdoba, Argentina, [5]Consejo Nacional de Investigaciones Científicas y Técnicas, CONICET, Instituto de Física La Plata, IFLP, Buenos Aires, Argentina

Magnetic hybrid nanomaterials offer promising properties for the advancement of nanoplatforms in cancer nanomedicine, particularly in drug delivery applications. These nanoplatforms can effectively respond to various stimuli present at the tumor site, such as pH and temperature fluctuations, allowing for controlled and triggered release of therapeutic payloads. In this study, we present a straightforward methodology for the synthesis of stable hybrid magnetic nanoplatforms (HMNP) based on Fe_3O_4 nanoparticles, *L*-cysteine (*L*-Cys), and hyaluronic acid (HA) as key constituents for the delivery of tamoxifen (TMX). The synthesized superparamagnetic HMNP, Fe_3O_4-*L*-Cys-HA, with a size of 11 nm, was successfully loaded with TMX. The incorporation of *L*-Cys showed superior interaction with the surface of Fe_3O_4 nanoparticles compared to other *L*-Cys derivatives explored as ligands. Consequently, *L*-Cys was selected for further functionalization with HA, providing the HMNP with active targeting properties toward CD44-overexpressed receptors. High loading efficiency of TMX (75%) was achieved *via* electrostatic interaction between the carboxylate groups exposed by the HMNP and the ammonium group of the TMX side chain. Efficient control in the TMX release towards different receptor media was observed. Notably, the release of TMX from HMNP-TMX was triggered under acidic pH and hyperthermia conditions, showcasing its responsiveness to both stimuli. Furthermore, enhanced anticancer activity of TMX against MDA-MB-231 breast cancer cells was observed when loaded into HMNP (IC_{50} almost 3-fold lower for HMNP-TMX compared to free TMX), indicating improved cell uptake of TMX-loaded HMNP in comparison to the free drug. Overall, pH/temperature dual-sensitive HMNP demonstrates promising potential as a nanoplatform for cancer nanomedicine, with prospects for magnetic hyperthermia therapy.

KEYWORDS

stimuli-responsive nanocarriers, hyaluronic acid, L-cysteine, controlled drug release, cancer nanomedicine

1 Introduction

Cancer remains a significant global health challenge, with increasing patient numbers despite advancements in anticancer strategies. In recent decades, there has been considerable interest in the development of biocompatible Fe-based magnetic nanomaterials (MNP) for biomedical applications, driven by their potential in both imaging and therapy (Tong and Kohane, 2016). Some of these materials have even received U.S. Food and Drug Administration (FDA) approval for clinical use, underscoring their relevance in medical settings (Huang et al., 2022). Particularly, Fe-oxide nanoparticles like Fe_3O_4 and Fe_2O_3 MNP have been extensively studied for cancer diagnosis, hyperthermia therapy (Parveen et al., 2012; Han et al., 2016), and as nanocarriers for drug delivery (Wan et al., 2016), owing to their superparamagnetic properties, T2-contrasting abilities, ease of surface functionalization, biocompatibility (Maurcio et al., 2013), easy preparation, and low cost (Mody et al., 2014).

The surface functionalization of MNP is crucial for achieving effective interaction with biological tissues while preserving their magnetic properties and minimizing cellular toxicity. The toxicity of MNP and their ability to bind to and be absorbed by cells are primarily determined by their surface functionalization (Busnel et al., 2005; Choi et al., 2012), as well as their physicochemical properties such as size (Li and Sha, 2008), surface charge (Toole, 2004; Laurent et al., 2008), and magnetic properties (El-Boubbou, 2018). Furthermore, in some cases, bare MNP have shown higher cellular toxicity than functionalized MNP (R. M. Patil et al., 2018; U. S. Patil et al., 2015). As a result of their high surface energy, MNP tend to exhibit some aggregation, and can interact with plasma proteins. These interactions may lead to opsonization and immune system clearance through the mononuclear phagocytic system, inducing a significant loss of MNP functionality against target cells. To avoid these undesired effects, the surface of the MNP has been often modified with biocompatible polymers or small molecules. This modification aims to enhance their stability, biocompatibility, drug loading efficiency, and interaction capability with the target cells/tissues. Therefore, the combination of superparamagnetic Fe-oxide nanoparticles and biocompatible surface-modification ligands is essential for producing nontoxic and stable nanomaterials for biomedical applications.

Small molecules have been employed in the synthesis of hybrid magnetic nanomaterials for drug delivery applications in cancer nanomedicine. For example, the choline kinase α1 inhibitor Ff35 has been conjugated with biomimetic MNP (Jabalera et al., 2019) for drug delivery and hyperthermia applications. Oleic acid has been used to stabilize and confer hydrophobic properties on Fe_3O_4 nanoparticles for further loading with an amphiphilic silane along with the photosensitizer chlorin e6 and coumarin 6. This theragnostic nanoplatform was evaluated for dual-mode imaging guidance and magnetic targeting enhancement in photodynamic therapy (Sun et al., 2017). Among the small molecules used for functionalization of MNP, amino acids (AA) have emerged as suitable ligands (Vieira et al., 2011; Mauricio et al., 2013; Schwaminger et al., 2015; Bruno et al., 2018) due to their natural affinity for biological systems and their ability to enhance the colloidal stability of MNP. The AA are naturally occurring molecules with an affinity for various biological systems that play a vital role in the body. Additionally, AA can contribute to the colloidal stability of MNP (Qu et al., 2012), influencing the synthesis of Fe-oxides, as well as the morphology and the particle size distribution (Cohen et al., 2008). Importantly, AA also provide active groups for interaction with functional molecules and can be directly incorporated into MNP without the need for a spacer agent (Ebrahiminezhad et al., 2013). There are several reports on the synthesis of AA-coated MNP using *L*-arginine, *L*-lysine, *L*-glutamine, glycine, *L*-tryptophan, *L*-tyrosine, and *L*-phenylalanine (Patron et al., 2008; Park et al., 2009; Viota et al., 2010; Jin et al., 2014; Nosrati et al., 2018a). Recently, methotrexate (Nosrati et al., 2018b) and tamoxifen (TMX) (Rostami et al., 2021) have been conjugated to *L*-lysine coated MNP for the inhibition of MCF-7 breast cancer cells. In addition, *L*-tyrosine-decorated MNP have been used as magnetic nanocarriers for TMX (Nosrati et al., 2018c).

In particular, *L*-cysteine (*L*-Cys) AA can bond to the hydroxylated surface of Fe-oxide nanoparticles, modifying their electrostatic properties (Vieira et al., 2011). This functionalization has also been proven to be appropriate for obtaining stable colloidal dispersions. Additionally, *L*-Cys can act as membrane-permeable antioxidant and free radical scavenger, serving as a precursor for glutathione synthesis, and having the ability to reduce oxidized proteins (Britos et al., 2019). Previously, our research group reported on the effect of incorporating *L*-Cys as a surface ligand of MNP. The presence of this AA improved the physical properties of the developed magnetic nanoplatform, such as hydrophilic behavior, dispersibility in aqueous media, and colloidal stability (Cadena et al., 2021). Moreover, the thiol group of *L*-Cys has been reported to provide the possibility of forming S-S bonds to achieve the conjugation of biomolecules with magnetic nanocarriers. Since the S–S bond can be broken under reductive conditions, this property has been exploited to trigger the drug release in the presence of a reducing agent (Xia et al., 2019).

Macromolecules have also been used in the development of hybrid nanoplatforms. Natural and synthetic biopolymers have been explored in the fabrication of nanocarriers for antitumor drug delivery (Price et al., 2018; Bhattacharya et al., 2023; Fazal et al., 2023; Zhu et al., 2023). For example, poly(*L*-lactic acid) (Hu et al., 2006), agar (Khan et al., 2023) or mixtures of chitosan/agarose (Pourmadadi et al., 2023), among others, have been used to prepare magnetic nanocarriers for drug delivery. However, these designed nanocarriers lack targeting properties to achieve the sites of action.

Targeting tumor cells specifically is essential to improve the efficacy of cancer treatment and minimize systemic toxicity (Alipoor et al., 2022; Tian et al., 2022). Nanotechnology-based approaches offer promising strategies for overcoming the bottlenecks of undirected biodistribution, unwanted side effects, and high-dose administration (García and Uberman, 2018). Nanocarriers can achieve satisfactory tumor targeting by utilizing the enhanced permeability and retention (EPR) effect-mediated passive targeting strategy. Furthermore, active targeting can enhance the effectiveness of nanocarriers by conjugating them with ligands that can specifically target overexpressed receptors in tumor cells (García, 2020; Torres et al., 2020). The inclusion of active targeting ligands on the surface of nanoparticles improves their targeting toward tumor cells (on-targets) rather than healthy cells (off-targets). In this regard, folic acid has been used as an active

targeting ligand. In general, this ligand has been conjugated with polymers, proteins, or small molecules for further functionalization of MNP. For example, Heidari Majd *et. al.* conjugated folic acid with polyethylene glycol in a synthetic pathway involving six steps, which allowed a hybrid magnetic nanocarrier loaded with TMX that showed significant growth inhibition of MCF-7 breast cancer cells (Majd et al., 2013). Uma Maheswari *et. al.* used bovine serum albumin to encapsulate folic acid, hesperidin, and eugenol with $CaFe_2O_4$ MNP (Uma Maheswari et al., 2021). Khalil *et. al.* developed a nanoplatform based on a bifunctional folic acid conjugated with aspartic acid-modified Fe_3O_4 (Khalil et al., 2022).

A simpler approach involves designing the hybrid nanoplatform using a multipurpose agent that serves as a stabilizer, drug-binding site, and also possesses targeting properties. Hyaluronic acid (HA) is a linear polysaccharide consisting of alternately repeated *N*-acetylglucosamine and glucuronic acid disaccharide, constituting a major part of the extracellular matrix and is synthesized by a wide variety of cells. This polymer has a strong affinity for cell-specific surface markers, such as the cluster determinant 44 (CD44) and the receptor for hyaluronate-mediated motility. These receptors, especially CD44, are overexpressed on the surface of several tumor cells.

Hence, the great selectivity of HA for CD44-overexpressing cancer cells has shown potential applications in targeted drug delivery therapies. Furthermore, HA exhibits superior physiochemical properties, such as a high water-binding capacity, non-toxicity, biodegradability, cytocompatibility, and non-immunogenicity (Kim et al., 2018). In addition, the carboxylate groups of HA can serve as binding sites for the incorporation of positively charged drugs. Therefore, HA has emerged as a promising candidate for targeted drug delivery systems.

Our research group already reported on the fabrication of hybrid magnetic nanoplatforms (HMNP) based on Fe_3O_4 nanoparticles, *L*-Cys and HA for controlled TMX release (Cadena et al., 2021). These HMNP exhibited high loading efficiency, hydrophilicity, magnetic responsiveness, hemocompatibility, and low cytotoxicity against normal breast cells (MCF-10A). TMX release from these platforms followed a sustained, diffusion-controlled mechanism, resulting in increased cytotoxicity against tumor cells (MCF-7) compared to free TMX.

Building upon our previous work, this study delves into the conjugation of *L*-Cys in the magnetic platform Fe_3O_4-L-Cys-HA and its impact on key physicochemical properties such as magnetic response, colloidal stability, and interaction with plasma proteins. We evaluated the interaction of Fe_3O_4 nanoparticles with *L*-Cys and its derivatives, including *L*-cystine (**1**), *L*-cystine methyl ester (**2**) and *N*-Boc-*L*-Cys methyl ester (**3**). The synthesis and characterization of Fe_3O_4 nanoparticles and their magnetic conjugates with AA derivatives and HA are detailed in the present study. Upon functionalization with HA, a HMNP was obtained and further loaded with TMX, selected as an anticancer drug model for breast cancer therapy. Our comprehensive characterization includes an analysis of TMX-loaded HMNP properties, fully characterizing the physicochemical properties of this magnetic nanoplatform, analyzing its pH and thermal responsiveness for TMX release, and evaluating the *in vitro* cytotoxicity against human breast carcinoma cell line MDA-MB-231. Overall, our findings demonstrate the potential of this stimuli-responsive nanoplatform for cancer nanomedicine, with implications for hyperthermia therapy.

2 Materials and methods

2.1 Materials

All chemicals were reagent-grade and were used as received from the manufacturer. Iron (III) chloride ($FeCl_3$, Merck®), iron (II) chloride ($FeCl_2$, Stream Chemicals), ammonium hydroxide (NH_4OH), sodium hydroxide (NaOH), hydrochloric acid (HCl 37% $w.w^{-1}$, sodium chloride (NaCl), *L*-Cys hydrochloride (Parafarm®), *L*-Cystine (Parafarm®), sodium salt of HA (NaHA, 97.4%) obtained from bacteria's fermentation (Parafarm®, MW ~ 1,500 kDa, intrinsic viscosity = 23.6 $dL.g^{-1}$), 3-dimethylaminopropyl-*N*′-ethylcarbodiimida, (EDAC, Sigma-Aldrich®), hydroxybenzotriazole (HOBt, Sigma-Aldrich®), potassium bromide anhydrous (KBr, Sigma-Aldrich®), sodium carbonate (Na_2CO_3, Sigma-Aldrich®), sodium bicarbonate ($NaHCO_3$, Sigma-Aldrich®), TMX citrate (Parafarm®) and D(+)-saccharose named as sucrose (Riedel-de Haën™). All solvents were distilled before use: methanol (Cicarelli®), absolute ethanol (Cicarelli®). Physiological solution (sodium chloride 0.9% $w.v^{-1}$), sterile dimethylsulfoxide (DMSO, Sigma-Aldrich®). Phosphate buffer solution (PBS) at pH 7.4 (to simulate plasmatic conditions) and acetate buffer solution (ABS) at pH 5.1 (to simulate intracellular endocytic conditions) were prepared according to the United States Pharmacopeia specifications (U.S. Pharmacopoeial Convention, 2015) using analytical grade reagents. Sodium carbonate-bicarbonate buffer (SCBB) at pH 8.8 (37°C) was prepared by mixing 90 mL of 0.1 M Na_2CO_3 and 10 mL of 0.1 M Na_2HCO_3, using analytical grade reagents (Dawson et al., 1989). All experiments were carried out with distilled and purified water or with ultra-pure water freshly obtained from a Milli-Q© system, and were performed under N_2 atmosphere, unless otherwise noted.

2.2 Cell culture

Human breast cancer cells (MDA-MB-231) were obtained from the American Type Culture Collection (ATCC) (Bethesda, MD, United States). Cells were seeded and maintained routinely in complete medium (CM) prepared with Dulbecco's Modified Eagle's Medium (DMEM) supplemented with 10% fetal bovine serum (FBS, Gibco®), 100 $U.mL^{-1}$ penicillin (Gibco®) and 100 $\mu g.mL^{-1}$ streptomycin (Gibco®). The cells were kept in a humidified 37°C incubator with 5% CO_2 incubator until passage 2–4, and then cultured for up to 4 additional passages if necessary.

2.3 Human plasma

Human plasma was gently supplied by the blood derivatives' pharmaceutical laboratory (Laboratory of Hemoderivatives, National University of Cordoba, UNC, Argentina). According to the information provided by the supplier, plasma samples were

obtained by two different procedures. On the one hand, blood was taken from healthy volunteers who directly donated their blood to the Blood Bank, Institute of Hematology and Hemotherapy, National University of Cordoba (Blood Law N° 22,990, Decree-law No. 1,330/2,004 National Executive Power, government of Argentina), where blood samples were collected in K_2EDTA-coated tubes (BD Vacutainer®) to prevent blood clotting. The tubes were centrifuged for 5 min at 4,000 rpm to pellet the cellular components and then the Blood Bank donated plasma samples to the Laboratory of Hemoderivatives (UNC), where the plasma was pooled and stored at −80°C. Hence, these plasma samples were obtained by centrifugation of human blood and named CHP. On the other hand, plasma samples were obtained by plasmapheresis either at the Blood Bank or at any other institution, which further donated the plasma to the Laboratory of Hemoderivatives (UNC). Apheresis refers to the process of separating cellular and soluble components of blood using a machine, which allows plasma to be obtained, from healthy volunteers, according to specific gravity and returned the cellular components back to the donor (Bianchi et al., 2021). These plasma samples obtained by apheresis were also pooled and stored at −80°C and named AHP. Immediately before the experiments, plasma samples were thawed and centrifuged at 12,000 × *g* at 4°C for 2 min to remove precipitated proteins that were pelleted, and supernatant plasmas were used for the experiments.

2.4 Step-by-step synthesis of Fe_3O_4 nanoparticles functionalized with *L*-cysteine and hyaluronic acid (Fe_3O_4-*L*-Cys-HA, named HMNP)

The synthesis of Fe_3O_4-*L*-Cys-HA was carried in sequential steps (Cadena et al., 2021). First, the magnetic core of magnetite (Fe_3O_4) nanoparticles was prepared. After that, modification with *L*-Cys was performed to obtain Fe_3O_4-*L*-Cys nanoparticles. Subsequently, these particles were functionalized with HA to synthetize the HMNP on the basis of the three components.

Synthesis of Fe_3O_4 nanoparticles: In a 100 mL three-neck round-bottom flask equipped with a mechanical stirrer and N_2 inlet, 75 mL of 0.7 M NH_4OH (molar ratio Fe:OH 3:22) were placed. Additionally, a mixed solution of ferrous and ferric ions (molar ratio 1:2) was prepared by dissolving 2.36 mmol $FeCl_2$ in 6 mL of HCl solution (3 M) and 4.73 mmol $FeCl_3$ in 3 mL of decarbonated ultra-pure water. The resulting solution of Fe^{2+}/Fe^{3+} was then quickly added to the NH_4OH solution under vigorous mechanical stirring (2,000 rpm), and the suspension was continuously stirred under N_2 for about 30 min. The formation of Fe_3O_4 nanoparticles was immediately observed by the presence of a black precipitate. The magnetic precipitate was collected with the help of an external magnet of neodymium and washed four times with a 1:1 mixture of water and ethanol (150 mL).

Modification of Fe_3O_4 nanoparticles with *L*-Cys to produce Fe_3O_4-*L*-Cys nanoparticles: Once the Fe_3O_4 nanoparticles were obtained, they were dispersed in 75 mL of ethanol, and a 60 mM solution of *L*-Cys (in SCBB, pH 8.8 at 37°C, 75 mL) was immediately added. The mixture was stirred mechanically (2,000 rpm) and heated at 37°C for 3 h. The magnetic powder was collected with an external magnet and washed four times with a mixture of water: ethanol 1:1 (150 mL). The as-obtained Fe_3O_4-*L*-Cys nanoparticles were dispersed in 110 mL of ultra-pure water for further functionalization with HA (Cadena et al., 2021).

Functionalization of Fe_3O_4-*L*-Cys nanoparticles with HA to produce the HMNP: For surface functionalization with HA, the activation of carboxylic acid groups of HA was carried out (Cadena et al., 2021). Consequently, 164 mg of NaHA and 40 mL of ultra-pure water were placed in a Schlenk tube. The mixture was stirred (5,000 rpm) and heated in an oil bath at 50°C. When the polymer was completely dispersed, 0.20 mmol of EDAC and 0.20 mmol of HOBt were added, and the mixture was allowed to react for 15 min. Finally, the activated polymer was added to a three-neck round-bottom flask containing 110 mL of Fe_3O_4-*L*-Cys conjugated dispersion under vigorous mechanical stirring (2,000 rpm). This mixture was allowed to react for 4 h at room temperature. The magnetic powder was collected with an external magnet of neodymium and washed four times with a mixture of water: ethanol 1:1 (150 mL). The HMNP, Fe_3O_4-L-Cys-HA, was dispersed in water and dialyzed twice against a solution of NaCl 0.9% w.v^{-1} for 48 h. After that, the black powder was collected in a Petri dish glass and dried at room temperature under air. Following this procedure, 482.3 mg of Fe_3O_4-*L*-Cys-HA were obtained, representing an overall yield of 32% (Cadena et al., 2021).

2.5 Physicochemical characterization of HMNP and its precursors

Characterization by powder X ray diffraction (PXRD) was performed using a PANalytical X'Pert Pro diffractometer (40 kV, 40 mA) in Bragg–Brentano reflection geometry with Cu Kα radiation (λ = 1.5418 Å). Data were gathered between 10° and 70° (2θ) in steps of 0.02 and a counting time of 24 s. The refinement of the crystal structure was performed by the Rietveld method using the Fullprof software. Fourier transform infrared (FT-IR) spectra were collected on an infrared microscope (Nicolet iN10, Thermo Scientific®, United States). Samples contained in KBr discs were scanned from 4,000 to 400 cm^{-1} and recording conditions were: normal resolution, sample scan, 64 s^{-1}. The spectra were recorded, processed and analyzed using the EZ Omnic ESP 8.3.103 software. The morphology of the nanoparticles was observed by transmission electron microscopy (TEM), conducted in a JEM-Jeol 1,120 operating at 80 kV, at the CIAP-IPAVE Research Institute, INTA, Córdoba, Argentina. The samples were prepared by dropping a dispersion of HMNP onto an ultrathin carbon-coated copper grid. TEM images were analyzed with J-Image software to calculate the particle size distribution. The average hydrodynamic diameter (d_H) of Fe_3O_4 and Fe_3O_4-*L*-Cys nanoparticles, and their respective size distribution by determination of the polydispersity index (PDI) were measured by dynamic light scattering (DLS), and electrokinetic potential (ζ) values were determined by electrophoretic light scattering (ELS), using a Malvern Zetasizer® Nano-ZS 90 equipment, and the results were processed with Zetasizer software version 7.12. The average particle sizes and size distribution are reported as the average of three independent measurements. Differential scanning calorimetry (DSC) and

thermogravimetric analysis (TGA) were performed in a thermal analysis instrument (Discovery series, TA® Instruments) equipped with a data station (Trios® software, v5.a.a.46572, TA® Instruments). DSC was performed on samples (0.9–1.7 mg) heated in non-hermetic aluminum pans with a pine hole, using heating ramp of 10°C.min^{-1} from 15°C to 200°C, under N_2 flux (50 mL.min^{-1}). TGA was performed on samples (approximately 2 mg) placed in open aluminum pans and heated from room temperature to 800°C under the conditions used in DSC analysis. UV-Vis determinations were carried out using an Agilent Technologies® Cary 60 spectrophotometer.

2.6 Interaction of Fe_3O_4 nanoparticles and Fe_3O_4-*L*-Cys with plasma

To study the interaction of unfunctionalized magnetite and *L*-Cys-functionalized magnetite, a previously reported methodology was used (Landgraf et al., 2015), with some modifications. Briefly, 450 µg Fe_3O_4 and 1,135 µg Fe_3O_4-*L*-Cys, equivalent to 450 µg of Fe_3O_4 were placed in 15 mL Falcon tubes and dispersed with 9 mL of different media: water or plasma (CHP and AHP). Each tube-content was divided into 3 vials to generate 3 different batches with the same volume at each sample per medium. The samples were then incubated for 1 h at 4°C. After incubation, nanosystem-plasma mixtures were transferred to new Falcon tubes containing 1 mL of 0.7 M sucrose cushion and centrifuged at 18,000 × *g* for 25 min at room temperature. The pellets were resuspended in 3 mL of PBS (pH 7.4) for washing, sonicated for 2 min and decanted for another 2 min. The samples were analyzed by DLS. The d_H and size distribution of Fe_3O_4 and Fe_3O_4-*L*-Cys nanoparticles were measured in PBS pH 7.4 at 25°C, using a Malvern Zetasizer® Nano-ZS 90 equipment, and the results were processed with the Zetasizer software version 7.12. All experiments were carried out in triplicate. The d_H values were expressed as mean ± standard deviation (SD).

2.7 Incorporation of TMX into HMNP

TMX was incorporated into the HMNP previously synthesized. For that, a protocol previously reported was used (Cadena et al., 2021), with some modifications. Briefly, a solution of 122 µM of TMX solution was prepared by dissolving 6.88 mg of TMX citrate in 100 mL of ultra-pure water. The sample was heated to 37°C and sonicated for 30 min to promote drug dissolution. An aliquot of 45 mL of TMX solution was placed in a flask, followed by the addition of 45 mg of HMNP. The mixture was dispersed by sonication and placed in an orbital shaker incubator (Benchtop Shaker Incubator TOU-120-2). The samples were continuously stirred at 100 rpm for 72 h at room temperature.

The magnetic solid was then removed with an external magnet of neodymium, and the supernatant was separated and reserved for spectrophotometric analysis by UV-visible determinations at 235 nm (Agilent Technologies® Cary 60). The HMNP-TMX was dispersed again in ultra-pure water to remove any TMX molecules superficially attached to the HMNP, and shacked for 15 min. After an external magnetic field was applying, HMNP-TMX were collected, and the supernatant was separated and reserved for further UV-Vis quantification. This procedure was repeated twice. Finally, the HMNP-TMX were placed in Petri dish glass, dried at room temperature under air, and stored under cover from light.

2.8 Drug loading efficiency

To determine the amount of TMX loaded into the HMNP, spectrophotometric determinations were carried out at 235 nm (Agilent Technologies® Cary 60). The amount of unloaded drug recovered in the external aqueous phase was quantified once the magnetic solid of HMNP-TMX was removed with a magnet of neodymium (Cadena et al., 2021). Previously, a TMX calibration curve was performed with known concentrations of TMX solutions (ε = 16,010 M^{-1}.cm^{-1}). A R^2 = 0.9943 was obtained, indicating a strong linear correlation between absorbance and TMX concentration. According to the amount of TMX initially incorporated to prepare the HMNP-TMX, the drug loading efficiency (DLE) was calculated (Eq. 1) as follows:

$$\boldsymbol{DLE}(\%) = \frac{\boldsymbol{TMX_i - TMX_u}}{\boldsymbol{TMX_i}} \times \mathbf{100} \quad (1)$$

where DLE (%) is the percentage of drug loading efficiency of TMX-loaded into HMNP, TMX_i is the initial amount of TMX incorporated during the preparation of HMNP-TMX and TMX_u is the amount of unloaded TMX determined by spectrophotometric analysis, using the calibration curve.

2.9 Interfacial properties in bio-relevant fluids

To study the interfacial properties of HMNP-TMX in bio-relevant fluids, measurements of d_H, PDI, and ζ were carried out by DLS and ELS analyses, respectively. Three different media were evaluated considering the properties of HMNP-TMX in dispersions to anticipate its behavior for upcoming release and cell culture studies. Buffer solutions (ABS at pH 5.1 and PBS at pH 7.4) and CM without antibiotics were selected. An amount of 240 µg of HMNP-TMX (equivalent to 200 µg of Fe_3O_4) was weighed and placed in microtubes, containing 2 mL of incubation medium. Subsequently, the samples were sonicated for 30 min, followed by a 5 min decantation before measurements at room temperature. Upon observation of sings of sedimentation, samples were subjected to hand shake for 15 s when necessary (Sandler et al., 2019; Avasthi et al., 2023).

2.10 Radiofrequency calorimetric response

The calorimetric response of the samples under a radiofrequency (RF) field was recorded (Bruvera et al., 2022). To achieve this, the powders were suspended in distilled water at concentrations of around 5 g.L^{-1}, with 15 min of ultrasound applied. Immediately after agitation, 500 µL of the suspension was placed in a Dewar flask inserted into the water-cooled coil of a Hüttinger 2.5 RF generator. The samples were subjected to a sinusoidal field of 300 kHz frequency and 57 kA.m^{-1} amplitude, while the temperature in the centre of the suspension was monitored using a Rugged TG-02 optical probe to obtain temperature (T) vs. time (t) curves. Three measurements were taken for each sample.

Using the slopes obtained $dT.dt^{-1}$, the specific absorption rate (SAR) was calculated for each sample under the applied RF field (Eq. 2):

$$SAR = \frac{c}{[MNP]} \times \frac{dT}{dt} \tag{2}$$

with c the specific heat of the suspension and $[MNP]$ the concentration of MNP as a mass-to-mass ratio.

2.11 Drug release studies

Aqueous dispersions of HMNP-TMX were subjected to drug release analysis. The release rate from an aqueous solution with an equivalent concentration of TMX was used as a reference. The experiments were performed in a bicompartmental diffusion device. A semi-permeable acetate cellulose membrane (12 kDa, Sigma-Aldrich®, United States) was placed between the donor and the receptor compartments. The donor compartment was filled with 4 mL of each dispersion and kept in contact with 10 mL of PBS pH 7.4 or ABS pH 5.1 (U.S. Pharmacopoeial Convention, 2015), which were used as receptor media. Samples of 1 mL of receptor medium were withdrawn at predetermined time intervals and replaced with equal amount of fresh medium. The experiments were performed in the absence of any applied magnetic field at 37°C (physiological temperature) and 43°C (hyperthermia condition), simulating extracellular plasma and tumor microenvironment conditions, respectively. The concentration of drug released was assayed spectrophotometrically (Agilent Technologies® Cary 60) at 235 nm. All experiments were carried out in triplicate and the sink conditions were maintained. The cumulative percentage of TMX released was calculated and expressed as a function of time. The results were expressed as the % average of the drug released in three independent determinations ± SD.

The release profiles of TMX from the HMNP-TMX and reference sample were statistically compared using the difference factor (f_1) and the similarity factor (f_2) (Eqs 3, 4, respectively). According to this methodology, an f_1 value greater than 15 and an f_2 value of 0–49 implies a difference between release profiles (Costa and Sousa Lobo, 2001):

$$f_1 = \frac{\sum_{t=1}^{n} |R_t - T_t|}{\sum_{t=1}^{n} Rt} \times 100 \tag{3}$$

$$f_2 = 50 \times log\left\{\left(1 + \left(\frac{1}{n}\right)\sum_{t=1}^{n} (R_t - T_t)^2\right)^{-0.5}\right\} \times 100 \tag{4}$$

where n is the number of sampling time points, $\sum$ is the sum of all time points and R_t and T_t are the cumulative percentages of the drug released at each of the n time points of the reference and test sample, respectively. The CV was less than 15% in all cases. Only one point after 85% of drug release was used for the equation.

2.12 Drug release kinetics by mathematical modelling

The mean release profiles were fitted according to common mathematical models as follows (Costa and Sousa Lobo, 2001):

$$\frac{M_t}{M_0} = K_z \times t \tag{5}$$

$$\frac{M_t}{M_0} = k_H \times t^{0.5} \tag{6}$$

$$\frac{M_t}{M_0} = k_P \times t^n \tag{7}$$

where M_t (%) is the percentage of drug released at time t, M_0 is the initial value of M_t, t is the time, n is the diffusion release exponent, and k_Z, k_H and k_P are the release coefficients corresponding to the kinetic models Zero order (Eq. 5), Higuchi (Eq. 6) and Korsmeyer-Peppas (Eq. 7), respectively.

2.13 *In vitro* cytotoxicity assay

The anticancer activity of TMX-loaded HMNP was studied against MDA-MB-231 breast cancer cells and compared with the cytotoxicity exhibited by free TMX. Cell viability was evaluated using the resazurin assay using alamarBlue®. This fluorometric/colorimetric method is based on the reduction of the blue compound resazurin (nonfluorescent) by viable cells to the pink-soluble product resorufin (fluorescent). As a growth indicator, the amount of resorufin produced is proportional to the number of viable cells due to mitochondrial respiration (Präbst et al., 2017). Briefly, exponentially growing cells were seeded in 96-well plates (5,000 cells/well) and allowed to grow in CM for 24 h until complete cell attachment. The growth medium was then discarded and replaced with alamarBlue®10% v.v $^{-1}$ dissolved in fresh CM containing the following treatments: free TMX and HMNP-TMX in a drug concentration range of 6.25–200 μM. Before exposure of cells to the treatments, both samples, initially in solid state, were reconstituted in sterile DMSO and diluted in the cell culture medium. The final concentration of DMSO did not exceed 0.8%. Treated cells were incubated for 24 h and the fluorescence intensity was measured on a microplate reader (Biotek®, excitation/emission = 535 nm/590 nm), as recommended by the manufacturer. Cell viability was expressed as a percentage respect to the viability exhibited by untreated cells (control). The results were expressed as mean ± standard error of the mean (SEM). All data were obtained from two independent experiments.

Half-maximal inhibitory concentration (IC_{50}) was calculated by the linear interpolation method using Eq. 8 (Caldwell and Yan, 2014).

$$IC_{50} = \frac{(50\% - low\%) \times (high[TMX] - low\,[TMX]}{high\% - low\%} + low\,[TMX] \tag{8}$$

where low% represents the highest percentage of cell growth inhibition less than 50%, high% represents the lowest percentage of cell growth inhibition greater than or equal to 50%, low $[TMX]$ represents the concentration of TMX that gives the low%, and high $[TMX]$ represents the concentration of TMX that gives the high%. Percentages of cell growth inhibition were determined as 100%—% cell viability.

2.14 Statistical analysis

Statistical analysis was performed by comparison of different experimental conditions according to the evaluation of mean values

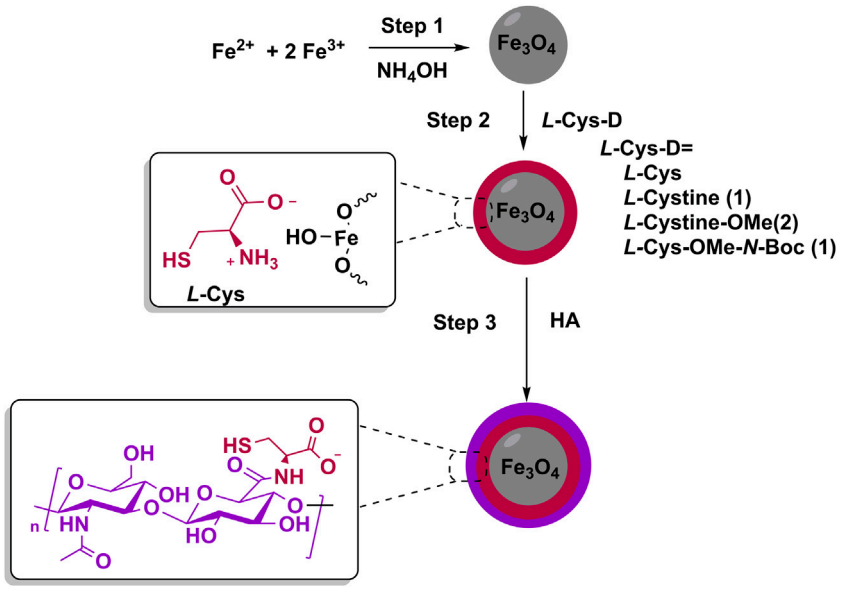

FIGURE 1
Schematic representation of the synthetic methodology used to obtain the hybrid magnetic nanoplatform (HMNP) based on magnetite (Fe_3O_4), *L*-cysteine (*L*-Cys), and hyaluronic acid (HA).

assessed by analysis of variance (one-way or two-way ANOVA) with the Bonferroni's *post hoc* test using Graph Pad® software. A p-value < 0.05 or less was considered significant.

3 Results

3.1 Synthesis and characterization of Fe_3O_4 nanoparticles and their magnetic conjugates with *L*-Cys and its derivates, and HA

To obtain a HMNP to be used as a nanocarrier for TMX in cancer nanomedicine, we chose the combination of magnetite (Fe_3O_4), *L*-Cys and HA, as magnetic core and organic ligands, AA and natural polymers, respectively. The synthetic pathway started with the preparation of the MNP core using the co-precipitation method by reacting a mixture of $FeCl_2$ and $FeCl_3$ with a large excess of NH_4OH (Step 1, Figure 1), achieving bare MNP with a mean diameter of (7 ± 2) nm. TEM analysis revealed spherical MNP with a significant degree of aggregation (Supplementary Figures S1A, S1B), which was also observed in the DLS analysis of an aqueous dispersion of MNP (d_H = (235 ± 22) nm, PDI = 0.37). The PXRD pattern exhibited the characteristic diffractogram of Fe_3O_4 phase with a face-centered cubic (fcc) structure at around 30.5°, 35.9°, 43.5°, 53.0°, 57.5°, and 63.1° (2Θ), corresponding to the (220), (311), (400), (422), (511), and (440) reflections, respectively (Supplementary Figures S1C) (Blanton and Gates-Rector, 2019). The saturation magnetization (*Ms*) measured by VMS analysis was of 62 emu.g^{-1} (Supplementary Figures S1D).

Once the Fe_3O_4 core was obtained, in a second step, *L*-Cys or its derivatives (*L*-Cys-D: **1**, **2** or **3**) were incorporated onto the surface of MNP (Step 2, Figure 1). Therefore, *L*-cystine (**1**) and the synthesized derivatives *L*-cystine methyl ester (**2**) and *N*-Boc-*L*-Cys methyl ester (**3**) were explored as surface ligands for Fe_3O_4 nanoparticles (Table 1).

Surface functionalization followed the methodology previously reported for *L*-Cys (Cadena et al., 2021), which involved incorporating a solution of *L*-Cys derivates (*L*-Cys-D) in SCBB (pH 8.8) into an ethanol dispersion of Fe_3O_4 nanoparticles. The surface modification of the MNP was examined by PXRD, FT-IR, TGA, and ζ measurements (Table 1).

The size and morphology of all functionalized MNP were analyzed using TEM micrographs (Supplementary Figure S3). In all samples, the MNP presented an almost spherical shape with a mean diameter ranging from 8 nm to 11 nm (Table 1), comparable to the size of the bare Fe_3O_4 MNP (Supplementary Figure S1). The amount of *L*-Cys-D incorporated onto the platforms was measured by TGA analysis (Figure 2A). *L*-Cys and *L*-cystine (**1**) demonstrated a strong interaction with Fe_3O_4, incorporating 60% and 67% of the organic ligand, respectively (Table 1). On the contrary, derivatives **2** and **3** incorporate only 10% and 9% of organic ligand onto MNP, respectively (Table 1).

The PXRD pattern of the functionalized MNP exhibited the characteristic peaks of the Fe_3O_4 phase (Figure 2B) (Vieira et al., 2011; Schwaminger et al., 2015). An additional phase was observed in the PXRD pattern for Fe_3O_4-*L*-Cys and Fe_3O_4-**1** (Figure 2B), which was well-matched with *L*-Cys peaks (2Θ = 18.80° and 28.50° peak), in full agreement with previous reports on this type of conjugated materials (Gawande et al., 2012).

Regarding FT-IR analysis (Figures 2C, D), the spectra of all MNP showed the typical low frequency bands of the spinel Fe_3O_4 at almost 600 cm^{-1} (Table 1; Figure 2C). For MNP modified with *L*-Cys or *L*-cystine (**1**), FT-IR spectra exhibited strong bands between 2,000 and 500 cm^{-1}, characteristic of organic ligands (Cadena et al., 2021). Both materials, Fe_3O_4-*L*-Cys and Fe_3O_4-**1**, showed an

10.3389/fnano.2024.1384605

TABLE 1 Characterization of Fe_3O_4 nanoparticles functionalized by *L*-Cys and its derivates.

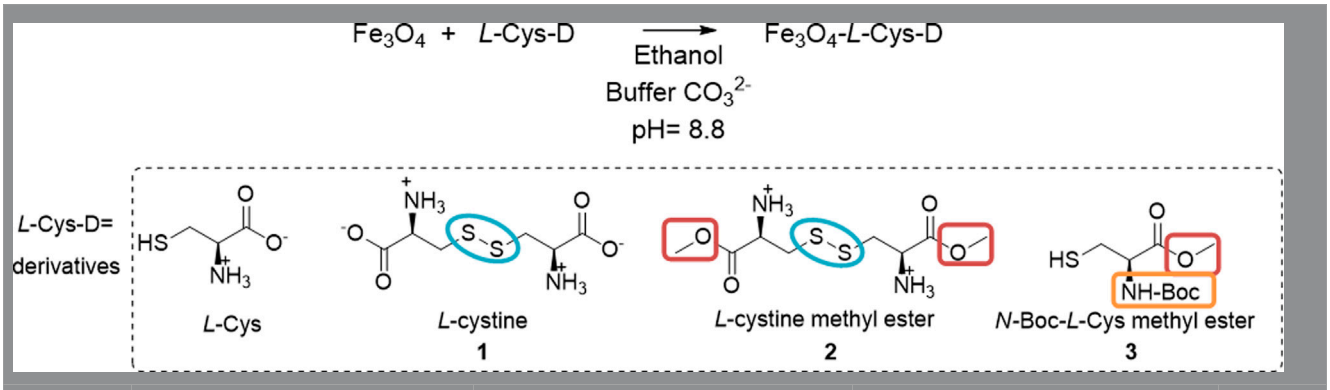

MNP	Mean diameter ± SD (nm)[a]	Ligand % (mg.100 mg MNP^{-1})[b]	FT-IR bands (cm^{-1})			ζ (mV)[c]
			ν Fe-O	ν C=O	δ NH_3^+	
Bare Fe_3O_4	7 ± 2	--	598	--	--	−23 ± 2
Fe_3O_4-*L*-Cys	8 ± 2	60	600	1,623	1,489	−22 ± 1
Fe_3O_4-*L*-**1**	11 ± 2	67	603	1,652	1,478	−11 ± 8
Fe_3O_4-*L*-**2**	9 ± 2	10	599	1,629	1,398	−14 ± 1
Fe_3O_4-*L*-**3**	9 ± 2	9	595	1,635	--	−19 ± 1

[a]Measurement by transmission electron microscopy (TEM). Images were analyzed with the J-Image software. SD: standard deviation.
[b]Determined by thermogravimetric analysis (TGA).
[c]Data obtained in samples dispersed in phosphate buffer solution (PBS at pH 7.4).

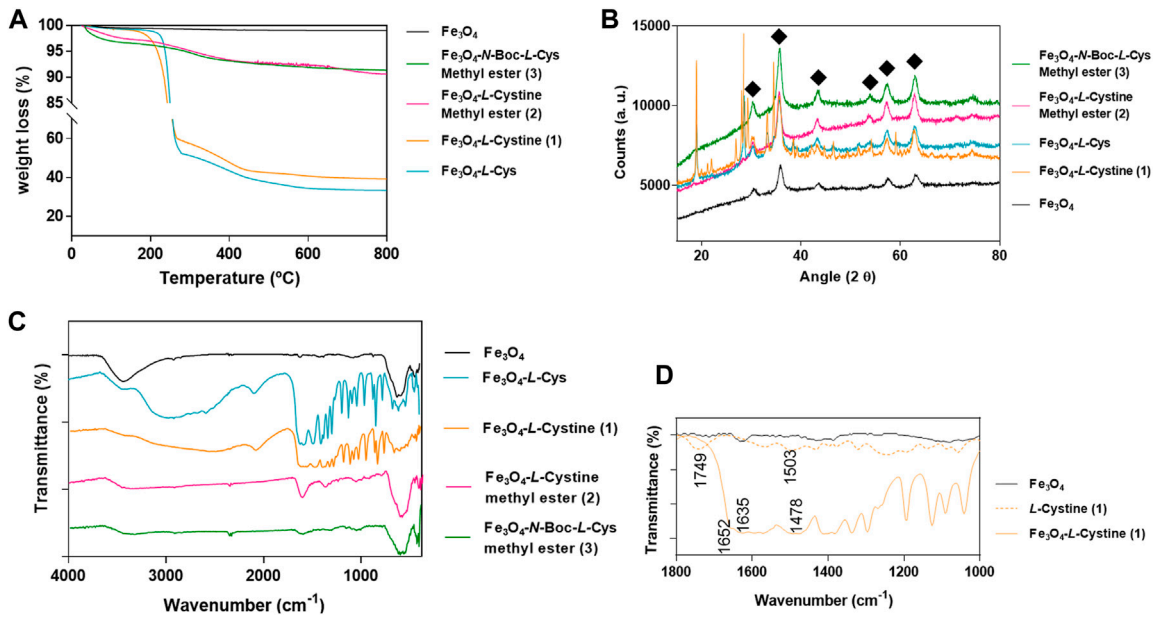

FIGURE 2
Characterization of Fe_3O_4 nanoparticles conjugated with *L*-cysteine (L-Cys) and its derivatives **1**, **2** and **3**: **(A)** TGA analysis; **(B)** PXRD diffractograms; **(C)** FT-IR spectra; and **(D)** a comparison between Fe_3O_4-**1** and its precursors (Fe_3O_4 MNP and *L*-cystine (**1**) between 1,800 and 1,000 cm^{-1}.

important broadening of the carboxylic group *stretch* vibration, as well as a shift in the wavenumber from 1,749 cm^{-1} to 1,652 cm^{-1}; together with a shift in the NH_3^+ group deformation band (1,503 cm^{-1} to 1,478 cm^{-1}) (Figure 2D) (Vieira et al., 2011; Schwaminger et al., 2015). Furthermore, a band at 2,590 cm^{-1} in Fe_3O_4-*L*-Cys could be associated with the presence of SH groups (Sangeetha and John, 2013). In contrast,

10.3389/fnano.2024.1384605

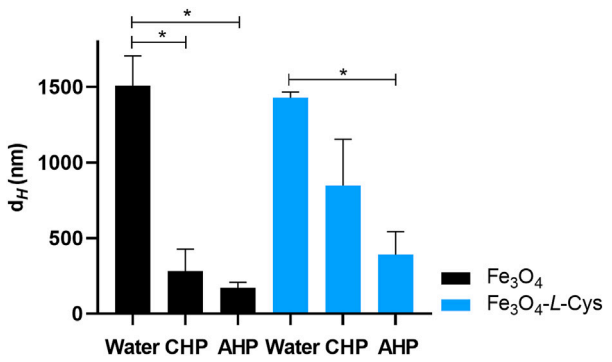

FIGURE 3
Average hydrodynamic diameter (d_H) of Fe_3O_4 nanoparticles and Fe_3O_4-*L*-Cys nanosystem after incubation in bio-relevant media: water, human plasma obtained by centrifugation of whole blood (CHP) and plasmapheresis (AHP). Asterisks represent a significant difference between the indicated groups ($p < 0.05$).

MNP modified with ligands **2** and **3** exhibited simpler FT-IR spectra in which C=O stretching (~1,630 cm^{-1}) of AA derivatives can be identified (Table 1; Figure 2C). After functionalization, the ζ values were measured at pH 8.8 for bare MNP and Fe_3O_4-*L*-Cys MNP, achieving values of ζ = 26.1 mV and ζ = −22.9 mV, respectively (Cadena et al., 2021). The determination of ζ in buffer PBS (pH 7.4) showed that all MNP exhibited a negative value of ζ < −11 mV (Table 1).

Given the efficient surface modification of MNP by *L*-Cys through the carboxylic acid group, as demonstrated by the results presented above, and considering that the other functional groups available in its derivates play a minor role in stabilizing the magnetite nanoparticles, *L*-Cys was selected as a ligand for further studies.

Taking into account the proposed biomedical applications for the nanoplatform and possible intravenous administration, the interactions of Fe_3O_4-*L*-Cys with human plasma proteins were studied and compared with the behavior shown by unfunctionalized Fe_3O_4 nanoparticles. The analysis was performed by DLS to measure d_H values after incubating Fe_3O_4 and Fe_3O_4-*L*-Cys in water, AHP, and CHP. The results are presented in Figure 3.

The results of the DLS analyses indicated that both Fe_3O_4 and Fe_3O_4-*L*-Cys exhibited important modifications in their d_H when incubated in different media. An increased aggregation of nanoparticles in water was observed, as shown by the high d_H values of Fe_3O_4 nanoparticles and Fe_3O_4-*L*-Cys after incubation in this medium (1,509 nm and 1,429 nm, respectively). The centrifugation process through a sucrose cushion applied to nanosystem-plasma mixtures allowed for the isolation of protein-nanoparticle complexes. Interestingly, the presence of a protein corona after incubation of samples in human plasma stabilized both Fe_3O_4 and Fe_3O_4-*L*-Cys nanoparticles, preventing aggregation of nanoparticles. This stabilization was indicated by significant reduced d_H values when incubated in AHP (170 nm and 390 nm for Fe_3O_4 and Fe_3O_4-*L*-Cys, respectively). These sizes were even lower than those obtained after incubation in CHP (283 nm and 849 nm, respectively). When comparing the results obtained for Fe_3O_4 and Fe_3O_4-*L*-Cys in plasma, a tendency of higher d_H values was observed for Fe_3O_4-*L*-Cys compared to Fe_3O_4 nanoparticles. However, incubation in high quality human plasma (AHP) improved stabilization of both samples and non-significant differences in their d_H values were observed (Figure 3).

3.2 Synthesis and physicochemical characterization of HMNP loaded with TMX

After synthesis and characterization of the magnetic core functionalized with the selected AA, the HMNP was prepared for TMX delivery by integrating HA into the Fe_3O_4-*L*-Cys nanoparticles, resulting in the Fe_3O_4-*L*-Cys-HA nanoplatform (Figure 1). The incorporation of HA was achieved using carbodiimide chemistry, employing an aqueous mixture of EDAC and HOBt reagents, as detailed in a previous work (Cadena et al., 2021). As was reported in this work, characterization studies confirmed the effective incorporation of HA into the nanomaterial.

The as-obtained HMNP was then loaded with TMX. Since HMNP exhibited negative ζ value at neutral pH (Cadena et al., 2021), positive charged TMX (pK_a = 8.9) established an electrostatic interaction with ionizable groups of HMNP. High % DLE was reached, achieving (75 ± 13) % of the drug loaded into the HMNP.

The TMX-loaded HMNP was further characterized by various spectroscopic techniques, together with a physical mixture (PM) of TMX and the HMNP Fe_3O_4-*L*-Cys-HA, which was prepared by simple mixing of powders of both components in the same proportion as present in the HMNP-TMX, for comparative purposes (Figure 4). The PXRD analysis revealed a new phase in the HMNP-TMX, indicated by a characteristic peak at 11.6°, similar to that observed for free TMX (Figure 4A). Additionally, the subsequent peaks at angles of 30.5°, 35.9°, 43.5°, 54.0°, 57.5°, and 63.1° correspond to the magnetic core present in the nanoplatform.

The TGA analysis performed for HMNP-TMX was compared with free TMX, unloaded HMNP, and the PM (Figure 4B). The TGA curve for free TMX exhibited two stages of thermal decomposition, the first at a temperature of 143°C and the second at 190°C. In the HMNP, a single degradation process was observed, starting at a temperature close to 153°C, which includes the decompositions of AH, *L*-Cys, and TMX. In comparison, the PM showed a lower thermal stabilization, and the TGA curve exhibited two stages of thermal decomposition, the first at a temperature of 146°C and the second at 180°C. Finally, the total organic component of the HMNP-TMX was of 9%. In the PM, higher amounts of organic components (15%) were observed.

The DSC analysis of TMX revealed a sharp peak at 151°C, corresponding to the drug fusion process (Figure 4C). Interestingly, in the HMNP-TMX, this peak was absent, in contrast to PM, in which a smaller peak, compared to the free drug, was observed at 143°C.

The morphology and size of the HMNP-TMX system were analyzed by TEM. The images showed that the particles in the HMNP-TMX were nearly spherical with a main diameter of (10 ± 3) nm. It was observed that this system exhibited a lower degree of aggregation compared to the nanoplatform without TMX (Figure 4E). The FT-IR analysis showed the characteristic bands of the nanoplatform (Figure 4D).

10.3389/fnano.2024.1384605

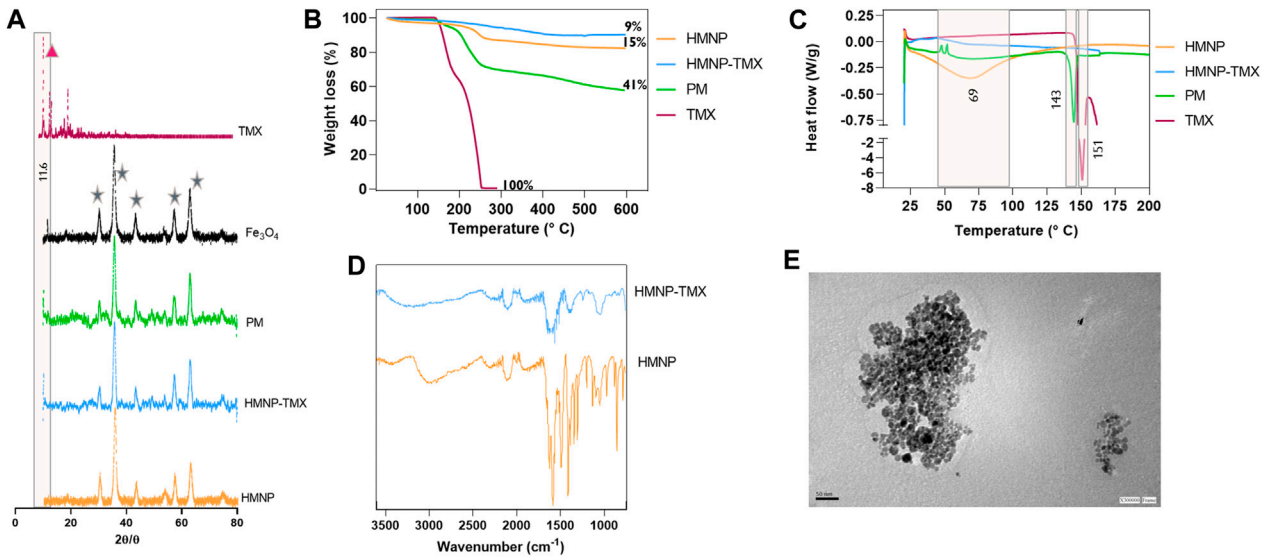

FIGURE 4
Caracterization of HMNP-TMX in comparison with its precursors and the physical mixture (PM) of TMX + nanoplatform by: **(A)** PXRD diffractograms; **(B)** TGA analysis, **(C)** DSC analysis, **(D)** FT-IR spectra, and **(E)** TEM images for HMNP-TMX. TMX: tamoxifen; Fe_3O_4: magnetite nanoparticles; HMNP: hybrid magnetic nanoplatform based on Fe_3O_4, *L*-cysteine and hyaluronic acid; HMNP -TMX: TMX-loaded into HMNP.

TABLE 2 Interfacial properties of freshly prepared dispersions of HMNP-TMX in different bio-relevant media.

Medium	d_H (nm)	PDI	ζ (mV)
ABS pH 5.1	839 ± 47	0.32 ± 0.02	−15 ± 2
PBS pH 7.4	254 ± 21	0.34 ± 0.03	−18 ± 1
CM	236 ± 32	0.51 ± 0.02	−7 ± 1

d_H: average hydrodynamic diameter; PDI: polydispersity index; ζ: electrokinetic potential; ABS: acetate buffer solution; PBS: phosphate buffer solution; CM: complete cell culture medium prepared with Dulbecco's Modified Eagle's Medium (DMEM), supplemented with 10% fetal bovine serum (FBS), without antibiotics; HMNP-TMX: tamoxifen-loaded hybrid magnetic nanoplatform.

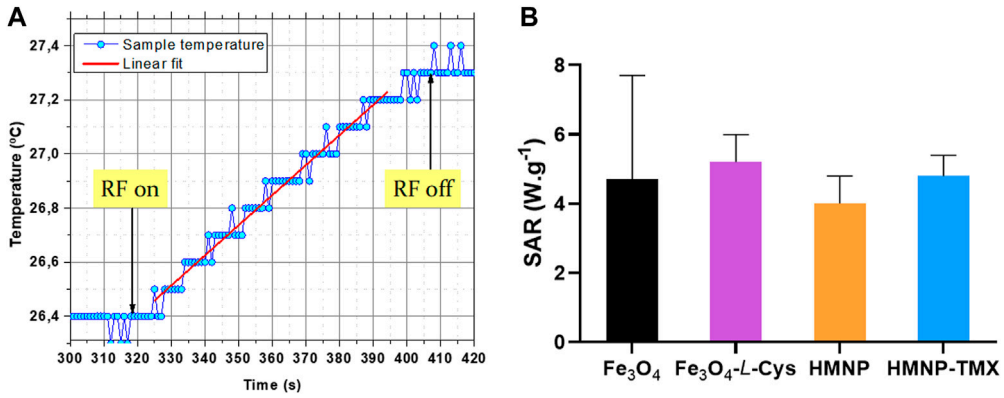

FIGURE 5
(A) Typical temperature vs. time curve for calorimetric experiments together with a lineal fitting of the data within the interval where the radiofrequency (RF) field is applied, in order to obtain the slope $dT.dt^{-1}$. **(B)** specific absorption rate (SAR) values for all samples expressed as dissipated power per unit mass of dry powder. TMX: tamoxifen; Fe_3O_4: magnetite nanoparticles; HMNP: hybrid magnetic nanoplatform based on Fe_3O_4, L-cysteine and hyaluronic acid; HMNP -TMX: TMX-loaded into HMNP.

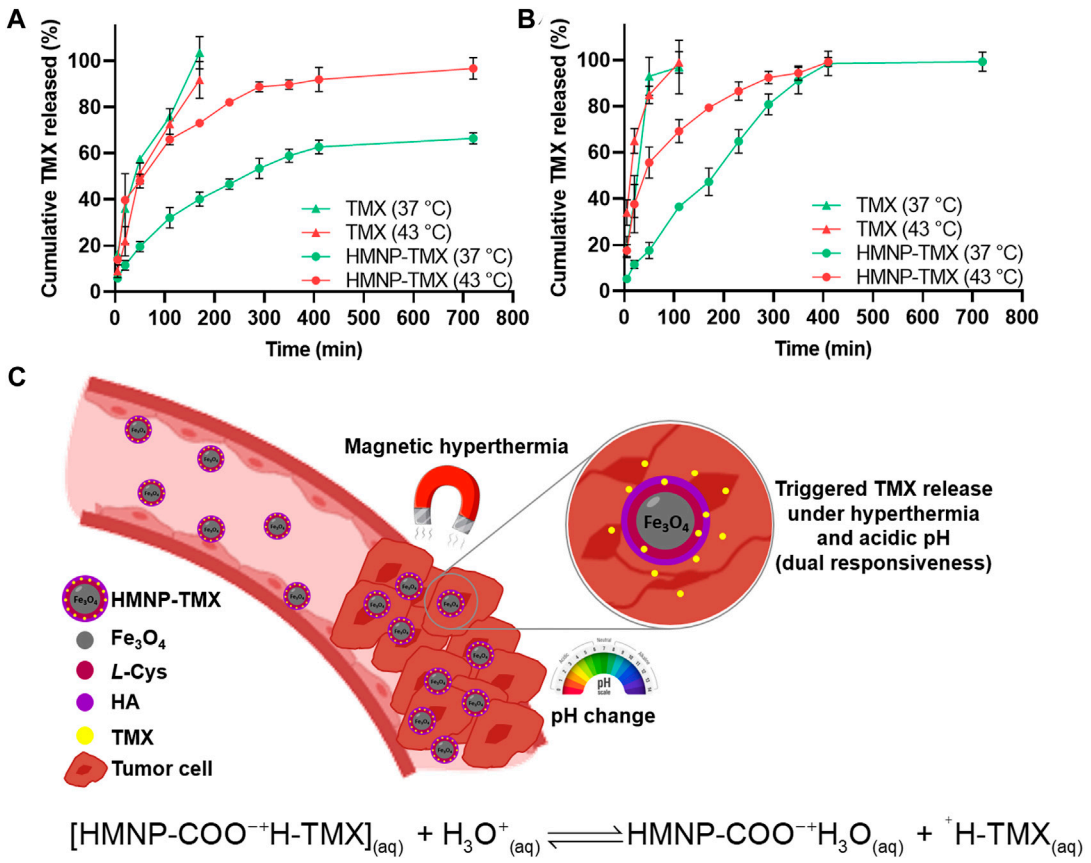

FIGURE 6
Release profiles of TMX from HMNP-TMX at 37°C and 43°C toward **(A)** phosphate buffer solution (PBS) at pH 7.4 and **(B)** acetate buffer solution (ABS) at pH 5, as release media. The release profiles of free TMX used as reference are also displayed. **(C)** Schematic depiction of the TMX-loaded HMNP and its dual responsiveness to both pH and temperature changes for triggering delivery of TMX. An equation is also presented to describe the pH-response behavior of HMNP-TMX for triggering release of TMX under acidic conditions. TMX is remarkably displaced in presence of hydronium ion. TMX: tamoxifen; Fe_3O_4: magnetite nanoparticles; *L*-Cys: *L*-cysteine; HA: hyaluronic acid; HMNP-TMX: TMX-loaded hybrid magnetic nanoplatform based on Fe_3O_4, *L*-Cys and HA.

To assess the dispersibility and colloidal stability of a dispersion of HMNP-TMX, DLS analyses were performed in bio-relevant fluids. Selected media were CM without antibiotics, PBS at pH 7.4 and ABS at pH 5.1 (Table 2). These media were chosen to simulate the conditions under which the samples were subjected in antitumor efficacy experiments when dispersed in cell culture medium and considering the media used for *in vitro* TMX release studies. It was observed that HMNP-TMX dispersed adequately in all media; however, signs of sedimentation were observed over time, indicating potential particle aggregation. Of note, they were easily re-dispersed with a brief 15 s hand-shaking. Therefore, DLS analyses were performed with fresh samples and measurements were performed immediately after preparation of the dispersions. As shown in Table 2, the d_H values of the HMNP-TMX-containing dispersions were considerably affected by the pH of the dispersion medium, being noticeably more aggregated in ABS at pH 5.1, as the d_H value (839 nm) was significantly higher than that obtained in PBS at pH 7.4 and CM (254 nm and 236 nm, respectively). A narrower size distribution was observed for samples dispersed in ABS and PBS (PDI < 0.34) compared to the CM used as dispersant (PDI ~0.5). All samples exhibited negative ζ, and lower values were obtained in buffer solutions (−15 mV and −18 mV for ABS and PBS, respectively) compared to that obtained in CM (−7 mV).

Considering hyperthermia applications, the behavior of different magnetite-containing samples under an RF field was evaluated. Figure 5A shows a typical temperature vs. time curve for the calorimetric experiments, along with a lineal fitting of the data within the interval where the RF field was applied. Figure 5B displays the SAR values for all the evaluated samples, expressed as the dissipated power per unit mass of dry powder. All the results cluster around 4 $W.g^{-1}$.

3.3 Release studies of TMX from HMNP-TMX

In vitro release profiles of TMX from HMNP-TMX toward PBS pH 7.4 and ABS pH 5.1, simulating physiological and lysosomal conditions, respectively, at 37°C and 43°C (physiological and hyperthermia temperatures, respectively), as receptor media were analyzed. Figure 6 shows cumulative percentages of TMX release as a function of the time. The release profiles of a reference sample of free TMX are also depicted.

TABLE 3 Kinetic data obtained from TMX release studies toward phosphate buffer solution (PBS) pH 7.4 and acetate buffer solution (ABS) pH 5.1 at two different temperatures, 37°C and 43°C, using Zero order, Higuchi and Korsmeyer-Peppas equations.

Temperature (°C)	Medium	Sample	Zero order		Higuchi		Korsmeyer-Peppas		
			k_Z	R^2	k_H	R^2	k_P	n	R^2
37	PBS pH 7.4	TMX	0.53	0.909	7.22	0.986	7.55	0.5	0.991
		HMNP-TMX	1.45	0.958	3.24	0.999	1.53	0.7	0.988
	ABS pH 5.1	TMX	1.66	0.997	15.43	0.959	6.15	0.7	0.975
		HMNP-TMX	0.26	0.995	4.51	0.968	1.72	0.6	0.986
43	PBS pH 7.4	TMX	0.60	0.938	8.03	0.984	2.88	0.7	0.989
		HMNP-TMX	0.43	0.845	5.91	0.939	7.90	0.5	0.940
	ABS pH 5.1	TMX	1.05	0.904	10.28	0.972	9.04	0.5	0.987
		HMNP-TMX	0.45	0.869	6.21	0.967	19.08	0.5	0.983

k_Z, k_H and k_P expressed as %.min^{-1}, %.min$^{-0.5}$ and %.k^{-n}, respectively. Experimental data correspond to 5%–60% of TMX, released. TMX: tamoxifen; HMNP-TMX: TMX-loaded hybrid magnetic nanoparticles.

The TMX was released in a controlled manner from HMNP-TMX towards both media (acidic- and neutral-pH environment) at the two temperatures evaluated (physiological and hyperthermia values); while the release of the TMX reference sample was faster, exhibiting similar profiles when comparing the different temperature at the same physiological pH (f_2 = 55.3). Noticeable *burst* effects were observed for free TMX, enabling approximately 20% of the drug to reach the receptor medium in the first 5 min toward both media at both temperatures. On the contrary, negligible *burst* effects were observed for the release of HMNP-TMX toward both media at 37°C, reaching approximately 5% of the TMX released in the first 5 min. When the medium was at higher temperature (43°C), *burst* effects were greater than those observed at physiological temperature, and approximately 15% of the drug was released in the first 5 min.

A lower leakage of the TMX release from HMNP-TMX toward physiological pH and temperature (Figure 6A) was achieved compared to the TMX release in an acidic environment (Figure 6B), which increased even at higher temperature. As observed, at any time toward PBS, and up to 400 min toward ABS, HMNP-TMX released the largest percentages of TMX at pH 5.1 compared to pH 7.4, reaching approximately 99% and 66% at 37°C, respectively (28.6 and 45.9 for f_1 and f_2 values, respectively), and the drug release increased even more at 43°C compared to 37°C (120.4 and 29.7 for f_1 and f_2 values at pH 7.4, respectively, and 119.3 and 28.4 for f_1 and f_2 values at pH 5.1, respectively), reaching almost 100% and 96% of drug release, respectively. The results suggest that HMNP-TMX actively participated in modulating drug release, with lower percentages of TMX released toward PBS pH 7.4 compared to the percentages of drug released toward ABS pH 5.1. This triggered effect produced at acidic pH and hyperthermia temperature indicated the stimuli-responsive behavior of HMNP-TMX.

Kinetic analyses of *in vitro* release data using Zero order, Higuchi and Korsmeyer-Peppas equations by mathematical modelling were performed to study the main mechanism of TMX transport through the magnetite-based HMNP.

The results of the kinetic data are summarized in Table 3. At physiological conditions, release data plotted as Higuchi and Korsmeyer-Peppas models were found to be fairly linear for both samples, free TMX and HMNP-TMX, which was also supported by their regression coefficient values (R^2 > 0.986 and R^2 > 0.988, respectively). Furthermore, n values in the range of 0.5–0.7 confirmed that the kinetics of TMX release from HMNP-TMX indicated a Fickian transport with a preponderant release mechanism controlled by drug diffusion. These results were in good correlation with the R^2 values obtained by applying the Higuchi model. Notably, in the case of HMNP-TMX, n values ≥ 0.5 suggested that even the main mechanism of drug release is diffusion-controlled, other mechanisms such as ionic exchange and the relaxation of polymer chains, etc. could also occur. At pH 5.1, kinetic release data were remarkably influenced by the temperature of the release medium. At 43°C, both release profiles were fitted to the Korsmeyer-Peppas model (R^2 = 0.987 and R^2 = 0.983 for TMX and HMNP-TMX, respectively) with a value of n close to 0.5, indicating a Fickian transport. In contrast, at 37°C, the release profiles were well fitted to Zero order (R^2 > 0.995), indicating an almost constant release rate.

3.4 *In vitro* cytotoxicity evaluation

The resazurin assay was used to evaluate whether TMX-loaded into HMNP could preserve its antitumor activity against triple negative human breast cancer cells. Because TMX is commonly used as a first-line treatment for breast cancer and considering it has reduced activity against cells that lack of estrogen receptors, the human breast carcinoma cell line MDA-MB-231 was selected as a challenging *in vitro* model for studying the cytotoxicity of HMNP-TMX and free TMX as reference sample. To study the antitumor activity of the developed nanoplatforms, cells were exposed to treatments for 24 h. Figure 7 shows the results of the resazurin assay. As observed, the cytotoxic activity of the drug from both samples was concentration-dependent in the range 25–200 μM. At

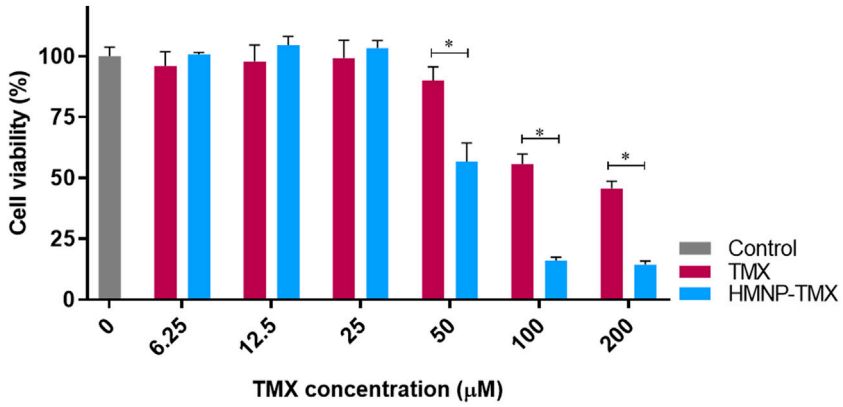

FIGURE 7
Cytotoxicity of free tamoxifen (TMX) and TMX-loaded HMNP (HMNP-TMX), at different concentrations, against MDA-MB-231 breast cancer cells. Cells were exposed to the treatments for 24 h. Cell viability was measured with the resazurin assay. Asterisks represent a significant difference between the indicated groups ($p < 0.05$).

concentrations ≤ 25 μM cell viabilities were similar to the control (untreated cells). Interestingly, HMNP-TMX exhibited significantly higher anticancer effects than TMX at the same concentrations ($p < 0.05$) as demonstrated by their mean IC_{50} values (157 μM and 58 μM for free TMX and HMNP-TMX, respectively).

4 Discussion

Overcoming limitations of current anticancer treatments has prompted the urgent need to find and develop novel strategies to address unmet clinical needs. Cancer nanomedicine presents a promising approach to overcome these shortcomings, as various tailor-made drug delivery nanosystems have been identified as promising nanocarriers. Nano-scale systems offer several advantages compared to their macro counterparts, including enhanced drug delivery to tumor tissue and, consequently, minimizing the side effects on the rest of the organism (García 2023; García et al., 2018). While several nanotechnologies-based systems for the delivery of TMX have already been reported to enhance the therapeutic performance of the drug for cancer therapy (Day et al., 2020; Chao et al., 2021), there are several challenges ahead in improving breast cancer treatment, particularly when patients are affected by triple-negative breast cancer cells, known for their more aggressive clinical course compared to other breast cancer subtypes (Mahmoud et al., 2022). Therefore, novel nanoformulations are needed to overcome these limitations, among which are nanosystems designed to release their payload only when exposed to a specific trigger stimulus at the tumor site, thus, preventing or minimizing drug release in the bloodstream and normal tissues to achieve optimal anticancer effects (García, 2022).

Here we present the design, development and evaluation of a hybrid nanoplatform exhibiting magnetic behavior, denoted as HMNP, comprised of Fe_3O_4, *L*-Cys and HA, featuring pH/temperature dual responsiveness to trigger the delivery of anticancer drugs such as TMX. HMNP was synthesized using a straightforward three-step methodology. The nanoplatform was engineered as a nanocarrier for cationic drugs such as, the selected anticancer drug, TMX, owing to its ability to interact with the carboxylic acid groups introduced by *L*-Cys and HA to the HMNP. Additionally, the presence of HA could facilitate targeted delivery of the nanoplatform to cancer cells.

The co-precipitation technique was employed to obtain the MNP using inexpensive and commercial reagents such as NH_4OH and inorganic salts of Fe^{2+} and Fe^{3+} (Laurent et al., 2008). This method has been widely used, and many clinically approved MNP have been prepared using this approach (El-Boubbou, 2018). Small nanoparticles composed of Fe_3O_4 were obtained, displaying the typical superparamagnetic behavior of Fe_3O_4-based MNP, with high value of *Ms* (Venosta et al., 2017).

As previously demonstrated, the incorporation of *L*-Cys into the nanoplatform improves certain properties such as aqueous dispersibility and colloidal stability (Cadena et al., 2021). Therefore, it was of interest to study the interaction between MNP with *L*-Cys and its derivatives (*L*-Cys-D) to fully understand the nature of the interactions between the Fe_3O_4 core and the functional groups present in AA derivatives. In the derivatives under study (Table 1), a progressive restriction of functional groups was performed to control the functionalities that could interact with the surface of Fe_3O_4 nanoparticles: *L*-cystine (**1**) presented thiol group protection by an S-S bond, leaving exposed the carboxylic acid and ammonium groups; *L*-cystine methyl ester (**2**) had only the ammonium group available; and *N*-Boc-*L*-Cys methyl ester (**3**) had only the thiol group available to interact with Fe_3O_4 nanoparticles. The characterization of the obtained Fe_3O_4-*L*-Cys-D samples revealed significant differences in the capacity of *L*-Cys derivatives as ligands. Firstly, it is important to note that the functionalization process did not alter the nature of the magnetic core, as the Fe_3O_4 phase was observed by PXRD in all Fe_3O_4-*L*-Cys-D samples.

The incorporation of *L*-Cys derivatives onto the surface of MNP strongly depended on the functional groups available in the organic ligands. Therefore, we were able to classify the organic ligands into two different groups. Ligands with available carboxylic acid groups, such as *L*-Cys and *L*-cystine (**1**), showed a strong interaction with Fe_3O_4 nanoparticles. This interaction was evidenced in the TGA

analyses, revealing a significant incorporation of the organic modifier in the final magnetic material [60% for *L*-Cys and 67% for *L*-cystine (**1**)], as shown in Table 1 and Figure 2A. Similar behavior was observed by Schwaminger *et. al.* for *L*-Cys (Schwaminger et al., 2015), and by Pušnik and cols. for *L*-aspartic acid and *L*-lysine (Pušnik et al., 2016), in which a large amount of AA was adsorbed onto the surface of MNP. However, in other Fe_3O_4-AA nanocarriers developed for TMX delivery, a lower coating of AA was achieved. A nanoplatform based on Fe_3O_4 superficially modified with *L*-tyrosine exhibited a weight loss of 7.5%, corresponding to the AA content (Nosrati et al., 2018a). Rostami et. al. determined the presence of 5.2% AA in a *L*-lysine-Fe_3O_4 nanocarrier (Rostami et al., 2021).

From PXRD (Figure 2B) and FT-IR (Figures 2C,D) analyses, the strong interaction of Fe_3O_4 with *L*-Cys and ligand **1** was confirmed. The PXRD pattern for Fe_3O_4-*L*-cystine (**1**) and Fe_3O_4-*L*-Cys exhibited the Fe_3O_4 phase along with ligand peaks in the diffractograms (Figure 2B). Comparative analysis of the FT-IR spectra of ligand **1** alone or bonded to Fe_3O_4 showed differences that could be attributed to the interaction between Fe_3O_4 nanoparticles and **1**. A notable broadening of carboxylic stretch vibrations was observed, as well as a shift in the wavenumber for the stretching of C=O bond from 1,739 cm^{-1} to 1,635 cm^{-1} in the Fe_3O_4-**1** nanosystem. Conversely, the band corresponding to NH_3^+ deformation showed a slight shift from 1,524 cm^{-1} to 1,478 cm^{-1}. Finally, the spectrum of Fe_3O_4-**1** nanosystem showed the typical low frequency band of the spinel Fe_3O_4 at near to 590 cm^{-1}, corresponding to Fe–O deformation in octahedral and tetrahedral sites (Silva et al., 2013). Similar results were observed for Fe_3O_4-*L*-Cys nanosystem (Cadena et al., 2021).

Different behavior was observed for derivatives **2** and **3**, in which carboxylic acid groups were blocked by ester bond formation. In these cases, minor functionalization of Fe_3O_4 nanoparticles was observed. For example, in TGA analyses, less than 10% of the organic content was detected (Table 1; Figure 2A). In PXRD analyses, only the characteristic peaks of the Fe_3O_4 phase were observed (Figure 2B), and the FT-IR spectra obtained for these samples were simpler and similar to Fe_3O_4 spectrum.

In general, the AA can interact with Fe-oxide MNP through various mechanisms: *i*) electrostatic interaction between zwitterionic molecules and amphoteric hydroxyl groups on metal oxides; *ii*) formation of covalent anhydrides between the carboxyl groups of AA and the OH surface groups of the MNP, and *iii*) specifically for *L*-Cys, an interaction is proposed through the thiol group and Fe-oxide surfaces, or the formation of *L*-Cys dimmer (*L*-cystine) which is capable of interacting through two carboxylic groups with the Fe-oxide surface (Cohen et al., 2008; Vieira et al., 2011; Schwaminger et al., 2015). At a pH value of 8.8, the acid-base equilibrium of *L*-Cys shifted towards the monoanionic form, where the amine functional group was protonated, and both carboxylic acid and thiol groups were deprotonated (Schwaminger et al., 2015). Furthermore, at this pH value, Fe_3O_4 nanoparticles exhibited a positive ζ of 26.1 mV (Jiang et al., 2012; Cadena et al., 2021). Thus, working at this pH conditions facilitated the electrostatic interaction between the MNP and the *L*-Cys through carboxylic acid groups.

Therefore, all characterization data suggest that COO^- groups in *L*-Cys and *L*-cystine (**1**) played an important role in coordinating the organic molecule over Fe-O surface, demonstrating that COO^- groups were prone to bind with Fe_3O_4 nanoparticles, possibly through the formation of covalent anhydrides (Baccile et al., 2013; Schwaminger et al., 2015). The negligible functionalization of Fe_3O_4 nanoparticles by ligands **2** and **3**; associated with COO^- group blockage by ester bond formation, pointed out the weak interaction between ammonium or thiolate groups and the surface of Fe_3O_4 nanoparticles. Thus, both *L*-Cys and *L*-cystine (**1**) were considered suitable candidates to be used as MNP modifying ligands. These results also demonstrated that the amino and thiol groups on *L*-Cys remained available for further chemical modifications of the nanoplatform.

Bearing in mind a possible intravenous administration of developed nanoplatform, an interfacial property of Fe_3O_4 and Fe_3O_4-*L*-Cys when dispersed in human plasma was studied to analyze their interaction with plasma proteins. After measuring the d_H by DLS (Figure 3), it was observed that nanoparticles-plasma complexes allowed stabilizing Fe_3O_4 and Fe_3O_4-*L*-Cys nanosystems upon interaction with plasma proteins, exhibiting smaller d_H compared to than that showed when dispersed in water. This could be explained because nanoparticles bind proteins, establishing a protein corona that constitutes a 'bio/nano interface' which prevent nanoparticle aggregation. A similar behavior has been also reported for Au@Fe_3O_4 Janus particles for which protein coronas were generated rapidly and these particles significantly reduced surface binding of coagulation proteins (Landgraf et al., 2015). As it has been previously reported (Tenzer et al., 2013), formation of plasma protein corona influences nanoparticle pathophysiology; therefore, this study was relevant since this 'bio/nano interface' affects the biological identity of the nanosystems in the bloodstream by determining their biocompatibility and transport.

Even some Fe_3O_4-AA conjugates have been used as nanocarriers in the treatment of cancer (Nosrati et al., 2018b; Nosrati et al., 2018c; Rostami et al., 2021), these functionalizations of MNP did not provide cancer-targeting properties. Therefore, to provide the final drug delivery nanoplatform targeting to cancer cells, HA was incorporated into the surface of Fe_3O_4-*L*-Cys nanoparticles (Figure 1). HA not only offered targeting properties, but also provided negative charge and served as drug-binding site.

The characterization of the resulting HMNP confirmed the successful integration of HA into the magnetic nanoplatform, resulting in the desired nanocarrier system. Subsequently, TMX was loaded into the HMNP. The percentage of DLE was determined by measuring the remaining solution of TMX after washing the obtained HMNP-TMX with ultra-pure water. The relatively high % DLE of TMX (75%) was comparable to that reported for other Fe_3O_4-containing nanoplatforms (Dutta et al., 2018), and it was even higher than that achieved with other hybrid nanocarriers based on poly(*L*-lactic acid) (Hu et al., 2006), *L*-tyrosine (Nosrati et al., 2018a), and folic acid-polyethylene glycol conjugated (Majd et al., 2013). The % DLE obtained was attributed to the large number of -COOH groups incorporated by both *L*-Cys and HA, which were likely to ionize and interact with TMX. It is noteworthy that the pH of the medium used during the interaction between TMX and HMNP (pH ≈ 7) favored the deprotonation of the -COOH groups, causing these groups to carry a negative charge (-COO^- groups), while TMX remained protonated.

To confirm the incorporation of the drug into the nanoplatform, a comprehensive characterization of the HMNP-TMX was performed (Figure 4). DSC analysis, TEM images, and FT-IR spectra provided valuable insights into the thermal behavior,

morphology, and chemical structure of the TMX-loaded HMNP. PXRD analysis showed a characteristic peak for TMX along with the Fe_3O_4 phase. The TGA analysis indicated an increase in the thermal stability of each of the precursors when integrated into the nanoplatform. DSC analysis demonstrated complete interaction between the TMX and the HMNP, as evidenced by the disappearance of the endothermic fusion of TMX. This was in contrast to the PM, which exhibited the fusion endotherm of the free drug. The absence of the sharp peak of the drug fusion in the DSC analysis of the HMNP-TMX, could be attributed to the effective immobilization or binding of TMX within the HMNP.

The TEM micrographs not only provided a visualization of the morphology and size of the HMNP-TMX but also highlighted the reduction in aggregation compared to the TMX-unloaded nanoplatform. A similar behavior was observed with an agar-coated iron nanoplatform, in which the dispersion of the particles significantly improved upon incorporating TMX (Khan et al., 2023).

To better understand the interfacial properties of HMNP-TMX, DLS analyses were conducted upon dispersion in bio-relevant fluids (Table 2). The CM without antibiotics was selected to simulate the conditions that HMNP-TMX undergo in antitumor efficacy experiments. Buffer solutions were chosen because they were the media used in *in vitro* TMX release studies, which simulated physiological and lysosomal conditions (García et al., 2022). In accordance to the results shown in Figure 3, the presence of proteins in CM, due to the FBS, allowed achieving the lowest d_H value, suggesting reduced aggregation of freshly prepared HMNP-TMX dispersion in this medium. This CM also influenced the ζ value, which could be explained by the protein-nanoparticle interactions. The pH values of both buffer solutions significantly affected the d_H of the HMNP-TMX in dispersion (Table 2). As observed, in ABS at pH 5.1, a higher d_H value was observed compared to that exhibited in PBS at pH 7.4, which was similar to that observed in CM. These results could be related to the pH-responsive behavior of HA, since it is an ionizable polymer and pH changes may have a significant impact on the performance of these type of hydrophilic polymers (Joseph, 2002); thereby inducing changes in the structure of HMNP as well as affecting the interaction of HMNP and TMX.

The magnetic behavior of the step-by-step samples obtained was evaluated under an RF field (Figure 5). The reported SAR values were consistent with the size of the MNP obtained by TEM analyses. For Fe_3O_4 nanoparticles of that size, the dominant dissipation mechanism is expected to be Néel relaxation, wherein the magnetic moment of the MNP flips between the two directions of the easy magnetization axis (Suto et al., 2009). This inference is, in turn, consistent with the similarity of SAR values across samples, given that the Néel mechanism is not dependent on the hydrodynamic radius of the MNP, which is modified with different functionalizations.

Overall, the detailed physicochemical characterization allowed us to comprehend the properties of TMX-loaded HMNP, providing valuable information for establishing its potential applications in drug delivery. Next, the biopharmaceutical and biological properties for cancer nanomedicine were studied.

The developed HMNP efficiently controlled the release of TMX under different release conditions (Figures 6A,B), acting as a promising nanocarrier for cancer nanomedicine. Consistent with the presented results, efficient control over TMX release has been previously reported for other HMNP based on Fe_3O_4 nanoparticles coated with *L*-lysine and loaded with this drug (Rostami et al., 2021), thus confirming the potential use of Fe_3O_4-containing nanoplatforms for controlled delivery of anticancer therapeutics. As expected, TMX reference sample was released at a faster rate, independently of the medium and temperature.

At physiological pH, the kinetic data of the HMNP fitted well to the Korsmeyer-Peppas model with *n* values near to or higher than 0.5 (Table 3), indicating a main Fickian transport in which the release of the drug was controlled by diffusion. However, other mechanisms such as ionic exchange and the relaxation of polymer chains could be also present. As described in Figure 6B and Table 3, at acidic pH, release profiles and their respective kinetic release were remarkably influenced by the temperature. Under physiological temperature, the kinetic data shifted, and release profiles fitted to Zero order model, indicating an almost constant release rate. The difference in kinetic release mechanisms could be attributed to the differential behavior exhibited by the HMNP-TMX when in contact with ABS pH 5.1 and PBS pH 7.4, according to the results presented in Table 2. The pH of the media not only influenced their d_H (smaller in PBS pH 7.4 compared to ABS pH 5.1, Table 2) but also it may have a significant impact on the performance of hydrophilic polymers containing ionizable groups in their molecular structure (Joseph, 2002), as is the case of HA, which may allow triggering release of TMX by ion exchange (Figure 6C).

Interestingly, the HMNP-TMX can trigger the drug release at acidic pH and hyperthermia temperature, confirming its responsiveness to both stimuli, as it was schematically depicted in Figure 6C. The increase in the percentage of TMX release from HMNP-TMX at higher temperature (43°C) compared to physiological temperature (37°C) demonstrated its thermal response and prospects for magnetic hyperthermia therapy. The responsiveness to temperature changes is particularly interesting in the treatment of cancer since tumor tissues usually show hyperthermia due to the rapid metabolism of cancer cells (Franco et al., 2021). Moreover, the HMNP-TMX may also be used to be remotely activated by an external magnetic field, triggering the drug release by magnetic-induced heating response thanks to the presence of superparmagnetic Fe_3O_4 nanoparticles. pH-sensitive nanocarriers can undergo conformational changes at acidic medium (Torres et al., 2020; García, 2022) and, in the case of hydrophilic polymers containing ionizable groups, pH changes affect their ionization state (Joseph, 2002), leading to the cargo release. This pH-sensitive behavior is of particular interest for the delivery of anticancer drugs because the extracellular pH of cancer tissues is slightly acidic due to the high metabolic activity of cancer cells. This allows nanocarriers to trigger drug release into the cytoplasm, optimizing cancer therapy. If the components of HMNP present acid-base ionizable groups, as shown by HA, responsiveness to pH changes can be achieved. The results showed that HMNP-TMX exhibited pH-responsive behavior when comparing the release profiles obtained at pH 7.4 and 5.1 (Figures 6A,B). As HMNP exhibited negative ζ

value at neutral pH, because under this condition it presented COO^- groups (pK_a value in the range 2.5–4.9), positively charged TMX interacted electrostatically with its ionizable groups (Cadena et al., 2021). Thus, at acidic pH, COO^- of HA were protonated, displacing the drug and, therefore, triggering its release (equation shown in Figure 6C).

Since TMX is mainly used to treat a specific type of breast cancer known as estrogen receptor-positive (Osborne et al., 2000; Dal Berto et al., 2021), it was decided to challenge the HMNP-TMX, and its biological performance was studied against MDA-MB-231 triple negative human breast cancer cells, a subtype clinically more aggressive than other breast cancer subtypes (Mahmoud et al., 2022). These cells lack estrogen receptor, progesterone receptor and human epidermal growth factor receptor 2.

As shown in Figure 7, TMX not only preserved its anticancer activity but also exhibited a significantly enhanced effect when loaded into HMNP. Similar results were previously reported for HMNP-TMX against estrogen receptor-positive MCF-7 cells (Cadena et al., 2021). However, drug concentrations to achieve anticancer effects were lower against MCF-7 cells compared to those required against MDA-MB-231 cells.

The significantly higher anticancer activity of HMNP-TMX compared to the free drug (IC_{50} of HMNP-TMX was 2.7-fold lower than the IC_{50} of free TMX) could be explained not only by the reduced size of HMNP-TMX that may positively impact on the anticancer activity by a passive targeting mechanism but also due to the presence of CD-44 receptors that may mediated its endocytosis (Chen et al., 2018).

Summing up, a pH/temperature dual-responsive nanoplatform based on biocompatible components was synthesized through a simple methodology using low toxicity materials. This nanoplatform showed promising properties for cancer nanomedicine due to its their nano-scale size, magnetic behavior, ability to control the drug release under physiological conditions, and the capability to trigger TMX release under acidic and hyperthermia conditions, resulting in enhanced anticancer activity. The nature of the interaction between the magnetic core and organic ligands was investigated, revealing the significance of carboxylic acid groups for effective surface functionalization of Fe_3O_4 nanoparticles. The HMNP efficiently loaded TMX with a high % DLE, attributed to the abundance of -COOH groups incorporated by both *L*-Cys and HA, which were likely to ionize and interact electrostatically with TMX at neutral pH. The physicochemical characterization of HMNP-TMX confirmed the successful incorporation of TMX into the HMNP, and its magnetic behavior was consistent with the size of the magnetic core. Overall, these promising properties warrant further exploration in other cancer cell lines and murine models, particularly in the presence of an external stimulus, to evaluate the magnetic-induced heating response for hyperthermia therapy.

Data availability statement

The original contributions presented in the study are included in the article/Supplementary Material, further inquiries can be directed to the corresponding authors.

Ethics statement

Ethical approval was not required for the studies on humans in accordance with the local legislation and institutional requirements because commercially available established cell lines were used and human plasma was gently supplied by the Laboratory of Hemoderivatives (UNC), in accordance with their own regulations.

Author contributions

JT: Investigation, Methodology, Writing–original draft, Data curation, Formal Analysis. DC: Investigation, Methodology, Writing–original draft, Data curation, Formal Analysis. RA: Data curation, Formal Analysis, Methodology, Writing–original draft. IB: Data curation, Formal Analysis, Methodology, Writing–original draft. PM: Data curation, Formal Analysis, Writing–original draft, Investigation. SM: Project administration, Resources, Writing–review and editing. MG: Project administration, Resources, Writing–review and editing, Conceptualization, Investigation, Methodology, Supervision, Visualization, Writing–original draft. PU: Conceptualization, Investigation, Methodology, Project administration, Resources, Supervision, Visualization, Writing–original draft, Writing–review and editing.

Funding

The author(s) declare that financial support was received for the research, authorship, and/or publication of this article. This work was supported by Agencia Nacional de Promoción Científica y Tecnológica–Fondo para la investigación Científica y Tecnológica (Grant number FONCyT-program, PICT 2018-3943, PICT 2019-2184, PICT 2019-0048, PICT 2021-0159); Consejo Nacional de Investigaciones Científicas y Técnicas de la República Argentina (Grant number: CONICET, PIP RD-20160120-0111, No: 00,271, PIBAA 2022-2023 No: 28720210101293CO, RESOL-2022-1930-APN-DIR#CONICET); Secretaría de Ciencia y Tecnología. Universidad Nacional de Córdoba (Grant numbers: SeCyT-UNC No: 05/CP15, Res. 366/16; SeCyT-Formar No: 33820190100091CB, Res. 233/2020; SeCyT-Consolidar No: 00705CB, Res. 411/2018; SECyT-Consolidar, No: 00705CB R. Secyt. 411/18). MG expresses gratitude for the funding received from the L'Oréal-UNESCO award "For Women in Science (FWIS)", in collaboration with the National Scientific and Technical Research Council of Argentina (CONICET).

Acknowledgments

MG , PU, SM, IB and PMZ, are members of CONICET's scientific career. JT thanks to CONICET for the doctoral fellowship and RA thanks to Argentinean National Interuniversity Council (CIN) for the fellowship awarded to conduct scientific initiation research activities. The authors wish to acknowledge the assistance of the CONICET and the National University of Cordoba (UNC, Argentina), both of which provided facilities for this work. The authors also acknowledge the assistance of Dr. Paula Bercoff (IFEG-CONICET-UNC, FAMAF) for her assistance in VMS analysis. Authors thank Mgter. Norma Maggia

(Lab. of Thermal Analysis, UNITEFA, CONICET-UNC) for technical assistance and perform of DSC-TGA runs. Also, authors would like to thank Laboratory of Hemoderivatives (UNC) for the provision of human plasma. MG deeply thanks the L'Oréal Foundation, L'Oréal Argentina, UNESCO, and CONICET for the FWIS award, fellowship category, which she won as an Argentine young investigator; the award was bestowed upon her in 2023 in the discipline described as 'Life Sciences'.

Conflict of interest

The authors declare that the research was conducted in the absence of any commercial or financial relationships that could be construed as a potential conflict of interest.

Publisher's note

Supplementary material

The Supplementary Material for this article can be found online at: https://www.frontiersin.org/articles/10.3389/fnano.2024.1384605/full#supplementary-material

References

Alipoor, R., Ayan, M., Hamblin, M. R., Ranjbar, R., and Rashki, S. (2022). Hyaluronic acid-based nanomaterials as a new approach to the treatment and prevention of bacterial infections. *Front. Bioeng. Biotechnol.* 10, 913912. doi:10.3389/fbioe.2022.913912

Avasthi, A., Caro, C., Luisa Garcia-Martin, M., and Leal, M. P. (2023). Deciphering the parameters to produce highly reproducible and scalable iron oxide nanoparticles. *React. Chem. Eng.* 8 (7), 1638–1653. doi:10.1039/D2RE00516F

Baccile, N., Noiville, R., Stievano, L., and Van Bogaert, I. (2013). Sophorolipids-functionalized iron oxide nanoparticles. *Phys. Chem. Chem. Phys.* 15 (5), 1606–1620. doi:10.1039/c2cp41977g

Bhattacharya, T., Preetam, S., Ghosh, B., Chakrabarti, T., Chakrabarti, P., Kumar Samal, S., et al. (2023). Advancement in biopolymer assisted cancer theranostics. *ACS Appl. Bio Mater.* 6 (10), 3959–3983. doi:10.1021/acsabm.3c00458

Bianchi, E., Mendoza, M., Paiaro, R., Fontana, D., and Beltrán, N. (2021). "Laboratory of hemoderivative: commitment to the quality of life. Social marketing campaign "donate plasma, donate smiles"," in *Applied social marketing and quality of life: case studies from an international perspective. 27–45. Applying quality of life research*. Editors M. Mercedes Galan-Ladero and R. G. Rivera (Cham: Springer International Publishing). doi:10.1007/978-3-030-83286-5_2

Blanton, T., and Gates-Rector, S. (2019). The powder diffraction file: a quality materials characterization database. *Powder Diffr.* 34 (4), 352–360. doi:10.1017/S0885715619000812

Britos, T. N., Castro, C. E., Bertassoli, B. M., Petri, G., Fonseca, F. L. A., Ferreira, F. F., et al. (2019). *In vivo* evaluation of thiol-functionalized superparamagnetic iron oxide nanoparticles. *Mater. Sci. Eng. C* 99 (September 2018), 171–179. doi:10.1016/j.msec.2019.01.118

Bruno, A. J., Correa, J. R., Peláez-Abellán, E., and Urones-Garrote, E. (2018). A novel method for the functionalization of aminoacids L-Glycine, L-glutamic acid and L-arginine on maghemite/magnetite nanoparticles. *J. Magnetism Magnetic Mater.* 456, 87–91. doi:10.1016/j.jmmm.2018.02.010

Bruvera, I. J., Actis, D. G., Soto, P., Blank, V., Roguin, L., Fernández van Raap, M. B., et al. (2022). Raiders of the lost SAR: radiofrequency cycles of magnetic nanoflowers inside a tumor. *J. Magnetism Magnetic Mater.* 563 (December), 169869. doi:10.1016/j.jmmm.2022.169869

Busnel, O., Carreaux, F., Carboni, B., Pethe, S., Le Goff, S. V., Mansuy, D., et al. (2005). Synthesis and evaluation of new ω-Borono-α-Amino acids as rat liver arginase inhibitors. *Bioorg. Med. Chem.* 13 (7), 2373–2379. doi:10.1016/j.bmc.2005.01.053

Cadena, C., Gerardo Gatti, D., Martín, S. E., Uberman, P. M., and García, M. C. (2021). Promising tamoxifen-loaded biocompatible hybrid magnetic nanoplatforms against breast cancer cells: synthesis, characterization and biological evaluation. *New J. Chem.* 45 (8), 4032–4045. doi:10.1039/d0nj04226a

Caldwell, G. W., and Yan., Z. (2014). "Rapidly distinguishing reversible and time-dependent CYP450 inhibition using human liver microsomes, Co-incubation, and continuous fluorometric kinetic analyses," in *Optimization in drug discovery:* in vitro *methods*. Editors G. W. Caldwell and Z. Yan (Totowa, NJ: Humana Press), 281–303. Methods in Pharmacology and Toxicology. doi:10.1007/978-1-62703-742-6_17

Chao, X., Zhao, L., Ma, N., Mou, Y., and Zhang, P. (2021). Nanotechnology-based drug delivery systems for the improved sensitization of tamoxifen. *J. Drug Deliv. Sci. Technol.* 61 (February), 102229. doi:10.1016/j.jddst.2020.102229

Chen, C., Zhao, S., Anand, K., and Freeman, J. W. (2018). The biology and role of CD44 in cancer progression: therapeutic implications. *J. Hematol. Oncol.* 11 (1), 64. doi:10.1186/s13045-018-0605-5

Choi, Ki Y., Saravanakumar, G., Park, J. H., and Park, K. (2012). Hyaluronic acid-based nanocarriers for intracellular targeting: interfacial interactions with proteins in cancer. *Colloids Surfaces B Biointerfaces* 99, 82–94. doi:10.1016/j.colsurfb.2011.10.029

Cohen, H., Gedanken, A., and Zhong, Z. (2008). One-step synthesis and characterization of ultrastable and amorphous Fe3O4 colloids capped with cysteine molecules. *J. Phys. Chem. C* 112 (39), 15429–15438. doi:10.1021/jp805090y

Costa, P., and Sousa Lobo, J. M. (2001). Modeling and comparison of dissolution profiles. *Eur. J. Pharm. Sci.* 13 (2), 123–133. doi:10.1016/S0928-0987(01)00095-1

Dal Berto, M., Tavares dos Santos, G., Vieira dos Santos, A., Oliveira Silva, A., Eduardo Vargas, J., Rafael José Vargas Alves, , et al. (2021). Molecular markers associated with the outcome of tamoxifen treatment in estrogen receptor-positive breast cancer patients: scoping review and *in silico* analysis. *Discov. Oncol.* 12 (1), 37. doi:10.1007/s12672-021-00432-7

Dawson, R. M. C., Elliott, D. C., Elliott, W. H., and Jones, K. M. (1989). *Data for biochemical research*. Third Edition, Third Edition. Oxford, New York: Oxford University Press.

Day, C. M., Hickey, S. M., Song, Y., Plush, S. E., and Garg., S. (2020). Novel tamoxifen nanoformulations for improving breast cancer treatment: old wine in new bottles. *Molecules* 25 (5), 1182. doi:10.3390/molecules25051182

Dutta, B., Shetake, N. G., Barick, B. K., Barick, K. C., Pandey, B. N., Priyadarsini, K. I., et al. (2018). pH sensitive surfactant-stabilized Fe3O4 magnetic nanocarriers for dual drug delivery. *Colloids Surfaces B Biointerfaces* 162 (February), 163–171. doi:10.1016/j.colsurfb.2017.11.054

Ebrahiminezhad, A., Ghasemi, Y., Rasoul-Amini, S., Barar, J., and Davaran, S. (2013). Preparation of novel magnetic fluorescent nanoparticles using amino acids. *Colloids Surfaces B Biointerfaces* 102 (February), 534–539. doi:10.1016/j.colsurfb.2012.08.046

El-Boubbou, K. (2018). Magnetic iron oxide nanoparticles as drug carriers: clinical relevance. *Nanomedicine* 13 (8), 953–971. doi:10.2217/nnm-2017-0336

Fazal, T., Murtaza, B. N., Shah, M., Iqbal, S., Rehman, R., Jaber, F., et al. (2023). Recent developments in natural biopolymer based drug delivery systems. *RSC Adv.* 13 (33), 23087–23121. doi:10.1039/D3RA03369D

García, M. C. (2022). "Chapter 17 - stimuli-responsive nanogels as promising carriers for controlled delivery of anticancer therapeutics," in *Stimuli-responsive nanocarriers. Seungpyo hong*. Editors V. Gajbhiye and K. R. Gajbhiye (Academic Press), 429–450. doi:10.1016/B978-0-12-824456-2.00005-9

García, M. C., Aloisio, C., Onnainty, R., and Ullio-Gamboa, G. (2018). Self-assembled nanomaterials. *Nanobiomaterials Nanostructured Mater. Biomed. Appl.*, 41–94. doi:10.1016/B978-0-08-100716-7.00003-9

García, M. C., Calderón-Montaño, J. M., Rueda, M., Longhi, M., Rabasco, A. M., López-Lázaro, M., et al. (2022). pH-temperature dual-sensitive nucleolipid-containing stealth liposomes anchored with PEGylated AuNPs for triggering delivery of doxorubicin. *Int. J. Pharm.* 619 (May), 121691. doi:10.1016/j.ijpharm.2022.121691

García, M. C., and Uberman, P. M. (2018). Nanohybrid filler-based drug-delivery system. *Nanocarriers Drug Deliv.*, 43–79. doi:10.1016/b978-0-12-814033-8.00002-3

García, C. M. (2020). "Nano-and microparticles as drug carriers," in *Engineering drug delivery systems* (Elsevier), 71–110.

Gawande, M. B., Velhinho, A., Nogueira, I. D., Ghumman, C. A. A., Teodoro, O. M. N. D., and Branco, P. S. (2012). A facile synthesis of cysteine-ferrite magnetic nanoparticles

for application in multicomponent reactions - a sustainable protocol. *RSC Adv.* 2 (15), 6144–6149. doi:10.1039/c2ra20955a

Hamdy Makhlouf, A. S., and Abu-Thabit, N. Y. (2023). "Chapter 17 - stimuli-responsive self-assembled nanocarriers based on amphiphilic block copolymers for cancer therapy," in *Applications of multifunctional nanomaterials. Ann rose abraham, 365–409. Micro and nano Technologies*. Editors S. Thomas and N. Kalarikkal (Elsevier). doi:10.1016/B978-0-12-820557-0.00016-3

Han, Lu, Zhang, X. Y., Wang, Yu L., Li, Xi, Yang, X. H., Huang, M., et al. (2016). Redox-responsive theranostic nanoplatforms based on inorganic nanomaterials. *J. Control. Release* 259, 40–52. doi:10.1016/j.jconrel.2017.03.018

Hu, F. X., Neoh, K. G., and Kang, E. T. (2006). Synthesis and *in vitro* anti-cancer evaluation of tamoxifen-loaded magnetite/PLLA composite nanoparticles. *Biomaterials* 27 (33), 5725–5733. doi:10.1016/j.biomaterials.2006.07.014

Huang, Y., Hsu, J. C., Koo, H., and Cormode, D. P. (2022). Repurposing ferumoxytol: diagnostic and therapeutic applications of an FDA-approved nanoparticle. *Theranostics* 12 (2), 796–816. doi:10.7150/thno.67375

Jabalera, Y., Sola-Leyva, A., Peigneux, A., Vurro, F., Iglesias, G. R., Vilchez-Garcia, J., et al. (2019). Biomimetic magnetic nanocarriers drive choline kinase alpha inhibitor inside cancer cells for combined chemo-hyperthermia therapy. *Pharmaceutics* 11 (8), 408. doi:10.3390/pharmaceutics11080408

Jiang, W., Chen, X., Niu, Y., and Pan, B. (2012). Spherical polystyrene-supported nano-Fe3O4 of high capacity and low-field separation for arsenate removal from water. *J. Hazard. Mater.* 243 (December), 319–325. doi:10.1016/j.jhazmat.2012.10.036

Joseph, S-N. (2002). Nuevas aportaciones galénicas a las formas de Administración, 27–65.

Jin, Y., Liu, F., Shan, C., Tong, M., and Hou, Y. (2014). Efficient bacterial capture with amino acid modified magnetic nanoparticles. *Water Res.* 50 (March), 124–134. doi:10.1016/j.watres.2013.11.045

Khalil, M., Haq, E. A., Dwiranti, A., Sunarwidhi Prasedya, E., and Kitamoto, Y. (2022). Bifunctional folic-conjugated aspartic-modified Fe3O4 nanocarriers for efficient targeted anticancer drug delivery. *RSC Adv.* 12 (8), 4961–4971. doi:10.1039/D1RA08776B

Khan, Z., Sattar, S., Abubakar, M., Javed Arshed, M., Aslam, R., Abbas Shah, S. T., et al. (2023). Preparation and *in vitro* evaluation of tamoxifen-conjugated, eco-friendly, agar-based hybrid magnetic nanoparticles for their potential use in breast cancer treatment. *ACS Omega* 8 (29), 25808–25816. doi:10.1021/acsomega.3c00844

Kim, J. H., Moon, M.Ju, Kim, D.Yi, Heo, S. H., and Jeong, Y. Y. (2018). Hyaluronic acid-based nanomaterials for cancer therapy. *Polymers* 10 (10), 1133. doi:10.3390/polym10101133

Landgraf, L., Christner, C., Storck, W., Schick, I., Krumbein, I., Dähring, H., et al. (2015). A plasma protein corona enhances the biocompatibility of Au@Fe3O4 Janus particles. *Biomaterials* 68 (November), 77–88. doi:10.1016/j.biomaterials.2015.07.049

Laurent, S., Forge, D., Port, M., Roch, A., Robic, C., Vander Elst, L., et al. (2008). Magnetic iron oxide nanoparticles: synthesis, stabilization, vectorization, physicochemical characterizations, and biological applications. *Chem. Rev.* 108 (6), 2064–2110. doi:10.1021/cr068445e

Li, J., and Sha, Y. (2008). A convenient synthesis of amino acid methyl esters. *Molecules* 13 (5), 1111–1119. doi:10.3390/molecules13051111

Mahmoud, R., Ordóñez-Morán, P., and Allegrucci, C. (2022). Challenges for triple negative breast cancer treatment: defeating heterogeneity and cancer stemness. *Cancers* 14 (17), 4280. doi:10.3390/cancers14174280

Majd, H., Asgari, D., Barar, J., Valizadeh, H., Kafil, V., et al. (2013). Tamoxifen loaded folic acid armed PEGylated magnetic nanoparticles for targeted imaging and therapy of cancer. *Colloids Surfaces B Biointerfaces* 106, 117–125. doi:10.1016/j.colsurfb.2013.01.051

Mauricio, W., Marcos, R., Ribeiro de Barros, H., Guilherme, M. R., Radovanovic, E., Rubira, A. F., et al. (2013). Synthesis of highly hydrophilic magnetic nanoparticles of Fe3O4 for potential use in biologic systems. *Colloids Surfaces A Physicochem. Eng. Aspects* 417, 224–229. doi:10.1016/j.colsurfa.2012.11.014

Mody, V. V., Cox, A., Shah, S., Singh, A., Bevins, W., and Parihar, H. (2014). Magnetic nanoparticle drug delivery systems for targeting tumor. *Appl. Nanosci. Switz.* 4 (4), 385–392. doi:10.1007/s13204-013-0216-y

Nosrati, H., Rashidi, N., Danafar, H., and Kheiri Manjili, H. (2018a). Anticancer activity of tamoxifen loaded tyrosine decorated biocompatible Fe3O4 magnetic nanoparticles against breast cancer cell lines. *J. Inorg. Organomet. Polym. Mater.* 28 (3), 1178–1186. doi:10.1007/s10904-017-0758-7

Nosrati, H., Salehiabar, M., Attari, E., Davaran, S., Danafar, H., and Kheiri Manjili, H. (2018b). Green and one-pot surface coating of iron oxide magnetic nanoparticles with natural amino acids and biocompatibility investigation. *Appl. Organomet. Chem.* 32 (2), e4069. doi:10.1002/aoc.4069

Nosrati, H., Salehiabar, M., Davaran, S., Danafar, H., and Kheiri Manjili, H. (2018c). Methotrexate-conjugated L-lysine coated iron oxide magnetic nanoparticles for inhibition of MCF-7 breast cancer cells. *Drug Dev. Industrial Pharm.* 44 (6), 886–894. doi:10.1080/03639045.2017.1417422

Osborne, C. K., Zhao, H., and Fuqua, S. A. W. (2000). Selective estrogen receptor modulators: structure, function, and clinical use. *J. Clin. Oncol.* 18 (17), 3172–3186. doi:10.1200/JCO.2000.18.17.3172

Park, Ja Y., Sook Choi, E., Ju Baek, M., and Lee, G.Ho (2009). Colloidal stability of amino acid coated magnetite nanoparticles in physiological fluid. *Mater. Lett.* 63 (3), 379–381. doi:10.1016/j.matlet.2008.10.057

Parveen, S., Misra, R., and Sahoo, S. K. (2012). Nanoparticles: a boon to drug delivery, therapeutics, diagnostics and imaging. *Nanomedicine Nanotechnol. Biol. Med.* 8 (2), 147–166. doi:10.1016/j.nano.2011.05.016

Patil, R. M., Thorat, N. D., Shete, P. B., Bedge, P. A., Gavde, S., Joshi, M. G., et al. (2018). Comprehensive cytotoxicity studies of superparamagnetic iron oxide nanoparticles. *Biochem. Biophysics Rep.* 13 (March), 63–72. doi:10.1016/j.bbrep.2017.12.002

Patil, U. S., Adireddy, S., Jaiswal, A., Mandava, S., Lee, B. R., and Chrisey, D. B. (2015). *In vitro/in vivo* toxicity evaluation and quantification of iron oxide nanoparticles. *Int. J. Mol. Sci.* 16 (10), 24417–24450. doi:10.3390/ijms161024417

Patron, L., Marinescu, G., Culita, D., Diamandescu, L., and Carp, O. (2008). Thermal stability of amino acid-(tyrosine and tryptophan) coated magnetites. *J. Therm. Analysis Calorim.* 91 (2), 627–632. doi:10.1007/s10973-006-8082-4

Pourmadadi, M., Ahmadi, M., and Yazdian, F. (2023). Synthesis of a novel pH-responsive Fe3O4/chitosan/agarose double nanoemulsion as a promising nanocarrier with sustained release of curcumin to treat MCF-7 cell line. *Int. J. Biol. Macromol.* 235 (April), 123786. doi:10.1016/j.ijbiomac.2023.123786

Präbst, K., Engelhardt, H., Ringgeler, S., and Hübner, H. (2017). "Basic colorimetric proliferation assays: MTT, WST, and resazurin," in *Cell viability assays: methods and protocols*. Editors D. F. Gilbert and O. Friedrich (New York, NY: Springer), 1–17. Methods in Molecular Biology. doi:10.1007/978-1-4939-6960-9_1

Price, P. M., Mahmoud, W. E., Al-Ghamdi, A. A., and Bronstein, L. M. (2018). Magnetic drug delivery: where the field is going. *Front. Chem.* 6 (December), 619. doi:10.3389/fchem.2018.00619

Pušnik, K., Peterlin, M., Kralj Cigić, I., Marolt, G., Kogej, K., Mertelj, A., et al. (2016). Adsorption of amino acids, aspartic acid, and lysine onto iron-oxide nanoparticles. *J. Phys. Chem. C* 120 (26), 14372–14381. doi:10.1021/acs.jpcc.6b03180

Qu, H., Ma, H., Zhou, W., and CharlesO'Connor, J. (2012). *In situ* surface functionalization of magnetic nanoparticles with hydrophilic natural amino acids. *Inorganica Chim. Acta* 389, 60–65. doi:10.1016/j.ica.2012.01.058

Rostami, S., Tafvizi, F., and Kheiri Manjili, H. R. (2021). High efficacy of tamoxifen-loaded L-lysine coated magnetic iron oxide nanoparticles in cell cycle arrest and anti-cancer activity for breast cancer therapy. *BioImpacts* 12 (4), 301–313. doi:10.34172/bi.2021.23337

Sandler, S. E., Fellows, B., and Thompson Mefford, O. (2019). Best practices for characterization of magnetic nanoparticles for biomedical applications. *Anal. Chem.* 91 (22), 14159–14169. doi:10.1021/acs.analchem.9b03518

Sangeetha, J., and John, P. (2013). Synthesis, characterization and antimicrobial property of Fe3O4-cys-HNQ nanocomplex, with L-cysteine molecule as a linker. *RSC Adv.* 3 (21), 8047–8057. doi:10.1039/C3RA00005B

Schwaminger, S. P., Fraga García, P., Merck, G. K., Bodensteiner, F. A., Heissler, S., Günther, S., et al. (2015). Nature of interactions of amino acids with bare magnetite nanoparticles. *J. Phys. Chem. C* 119 (40), 23032–23041. doi:10.1021/acs.jpcc.5b07195

Silva, V. A. J., Andrade, P. L., Silva, M. P. C., Bustamante, A. D., De Los Santos Valladares, L., and Albino Aguiar, J. (2013). Synthesis and characterization of Fe3O4 nanoparticles coated with fucan polysaccharides. *J. Magnetism Magnetic Mater.* 343, 138–143. doi:10.1016/j.jmmm.2013.04.062

Sun, X., Dong, B., Xu, H., Xu, S., Zhang, X., Lin, Y., et al. (2017). Amphiphilic silane modified multifunctional nanoparticles for magnetically targeted photodynamic therapy. *ACS Appl. Mater. Interfaces* 9 (13), 11451–11460. doi:10.1021/acsami.7b00647

Suto, M., Hirota, Y., Mamiya, H., Fujita, A., Kasuya, R., Tohji, K., et al. (2009). Heat dissipation mechanism of magnetite nanoparticles in magnetic fluid hyperthermia. *J. Magnetism Magnetic Mater.* 321 (10), 1493–1496. doi:10.1016/j.jmmm.2009.02.070

Tenzer, S., Docter, D., Kuharev, J., Anna, M., Fetz, V., Hecht, R., et al. (2013). Rapid Formation of plasma protein corona critically affects nanoparticle pathophysiology. *Nat. Nanotechnol.* 8 (10), 772–781. doi:10.1038/nnano.2013.181

Tian, H., Zhang, T., Qin, S., Huang, Z., Zhou, Li, Shi, J., et al. (2022). Enhancing the therapeutic efficacy of nanoparticles for cancer treatment using versatile targeted strategies. *J. Hematol. Oncol.* 15 (1), 132. doi:10.1186/s13045-022-01320-5

Tong, R., and Kohane, D. S. (2016). New strategies in cancer nanomedicine. *Annu. Rev. Pharmacol. Toxicol.* 56 (1), 41–57. doi:10.1146/annurev-pharmtox-010715-103456

Toole, B. P. (2004). Hyaluronan: from extracellular glue to pericellular cue. *Nat. Rev. Cancer* 4 (7), 528–539. doi:10.1038/nrc1391

Torres, J., Dhas, N., Longhi, M., and MónicaGarcía, C. (2020). Overcoming biological barriers with block copolymers-based self-assembled nanocarriers. Recent advances in delivery of anticancer therapeutics. *Front. Pharmacol.* 11, 593197. doi:10.3389/fphar.2020.593197

Uma Maheswari, P., Muthappa, R., Bindhya, K. P., and Meera Sheriffa Begum, K. M. (2021). Evaluation of folic acid functionalized BSA-CaFe2O4 nanohybrid carrier for the controlled delivery of natural cytotoxic drugs hesperidin and eugenol. *J. Drug Deliv. Sci. Technol.* 61 (February), 102105. doi:10.1016/j.jddst.2020.102105

U.S. Pharmacopoeial Convention (2015). *The United States Pharmacopeia. The national formulary. The national formulary and dispensing information (33)*. Rockville, Maryland: Rockville, Md: United States Pharmacopeial Convention, Inc. c1979- https://search.library.wisc.edu/catalog/999509774402121.

Venosta, L., Bracamonte, M. V., Rodríguez, M. C., Jacobo, S. E., and Bercoff, P. G. (2017). Comparative studies of hybrid functional materials based on different carbon structures decorated with nano-magnetite. Suitable application as platforms for enzyme-free electrochemical sensing of hydrogen peroxide. *Sensors Actuators B Chem.* 248 (September), 460–469. doi:10.1016/j.snb.2017.03.159

Vieira, A. P., Berndt, G., De Souza Junior, I. G., Di Mauro, E., Paesano, A., De Santana, H., et al. (2011). Adsorption of cysteine on hematite, magnetite and ferrihydrite: FT-IR, mössbauer, EPR spectroscopy and X-ray diffractometry studies. *Amino Acids* 40 (1), 205–214. doi:10.1007/s00726-010-0635-y

Viota, J. L., Arroyo, F. J., Delgado, A. V., and Horno, J. (2010). Electrokinetic characterization of magnetite nanoparticles functionalized with amino acids. *J. Colloid Interface Sci.* 344 (1), 144–149. doi:10.1016/j.jcis.2009.11.061

Wan, J., Yuan, R., Zhang, C., Wu, N., Yan, F., Yu, S., et al. (2016). Stable and biocompatible colloidal dispersions of superparamagnetic iron oxide nanoparticles with minimum aggregation for biomedical applications. *J. Phys. Chem. C* 120 (41), 23799–23806. doi:10.1021/acs.jpcc.6b06614

Xia, K.-kun, Lyu, Y., Harrison, S., Wu, J., Stratton, H., Zhang, S. j., et al. (2019). Nanocarriers of Fe3O4 as a novel method for delivery of the antineoplastic agent doxorubicin into HeLa cells *in vitro*. *Front. Oncol.* 9 (April), 250. doi:10.3389/fonc.2019.00250

Zhu, J., Wang, J., and Li, Y. (2023). Recent advances in magnetic nanocarriers for tumor treatment. *Biomed. Pharmacother.* 159 (March), 114227. doi:10.1016/j.biopha.2023.114227